



1 **Predictive mapping of organic carbon stocks and accumulation rates**
2 **in surficial sediments of the Canadian continental margin**

3

4 Graham Epstein^{1*}, Susanna D. Fuller², Dipti Hingmire³, Paul G. Myers⁴, Angelica Peña⁵, Clark Pennelly⁴
5 & Julia K. Baum¹

6

7 ¹Department of Biological Sciences, University of Victoria, Victoria, British Columbia, Canada, V8P 5C2

8 ²Oceans North, Halifax, NS B3J 1E6, Canada.

9 ³School of Earth and Ocean Sciences (SEOS), University of Victoria, Victoria, British Columbia, Canada,
10 V8P 5C2

11 ⁴ Department of Earth and Atmospheric Sciences, University of Alberta, Edmonton, Canada, AB T6G 2E3

12 ⁵ Institute of Ocean Sciences, Fisheries and Ocean Canada, Sidney, British Columbia, Canada, V8L 4B2

13

14 *Corresponding author: Email - grahamepstein@uvic.ca

15



16 **Abstract**

17 The quantification and mapping of surficial seabed sediment organic carbon has wide-scale
18 relevance across marine ecology, geology and environmental resource management, with carbon
19 densities and accumulation rates being a major indicator of geological history, ecological function,
20 and ecosystem service provisioning, including the potential to contribute to nature-based climate
21 change mitigation. While global mapping products can appear to provide a definitive
22 understanding of the spatial distribution of sediment carbon, there is inherently high uncertainty
23 when making estimates at this scale. Finer resolution national maps which utilise targeted data
24 syntheses and refined spatial data products are therefore vital to improve these estimates. Here,
25 we report a national systematic review of data on organic carbon content in seabed sediments
26 across Canada and combine this with a synthesis and unification of best available data on
27 sediment composition, seafloor morphology, hydrology, chemistry, geographic setting and
28 sediment mass accumulation rates within a machine learning mapping framework. Predictive
29 quantitative maps of mud content, sediment dry bulk density, and organic carbon content, density
30 and accumulation, were each produced along with cell specific estimates of their 95% confidence
31 interval (CI) bounds at 200 m resolution across 4,489,235 km² of the Canadian continental margin
32 (92.6% of the seafloor area above 2,500 m). Fine-scale variation in carbon stocks was identified
33 across the Canadian continental margin, particularly in the Pacific and Atlantic Ocean regions.
34 Carbon accumulation was predicted to be concentrated in coastal areas, with the highest rates in
35 the Gulf of St Lawrence and Bay of Fundy. Overall, we estimate the standing stock of organic
36 carbon in the top 30 cm of surficial seabed sediments across the Canadian shelf and slope to be
37 10.7 Gt (95% CI 6.6 – 16.0 Gt), and accumulation at 4.9 Mt per year (95% CI 2.6 – 9.3 Mt y⁻¹).
38 Increased *in-situ* sediment data collection and higher precision in spatial environmental data-
39 layers could significantly reduce uncertainty and increase accuracy in these products over time.

40

41 **1. Introduction**

42 The organic carbon contained in seafloor sediments has a major influence on global carbon cycles
43 and earth's climate (Hülse et al., 2017; Bauer et al., 2013). Seabed sediments have been
44 estimated to accumulate approximately 126–350 Mt of organic carbon per year (Keil, 2017;
45 Berner, 1982) and contain 87 Gt of organic carbon in their top 5 cm (Lee et al., 2019), 168 Gt in
46 the top 10 cm (LaRowe et al., 2020a) and up to ~2,300 Gt in the top 1 m (Atwood et al., 2020),
47 with the latter being equivalent to nearly twice that of soils on land. Continental shelves have the



48 highest concentrations of sediment carbon across the global ocean, covering only 5-8% of the
49 marine area but an estimated 15-19% of surficial organic carbon stocks (LaRowe et al., 2020a;
50 Atwood et al., 2020) and 80% of annual carbon burial (Bauer et al., 2013; Burdige, 2007).
51 Continental margin zones (continental shelves and slopes) also contain the largest spatial
52 variation in organic carbon densities due to highly heterogenous geological, geographic, biological
53 and oceanographic settings (Smeaton et al., 2021; Diesing et al., 2017, 2021; Atwood et al.,
54 2020). They are also subjected to high levels of human activity, being impacted by many coastal
55 and marine industries including fishing, shipping, energy generation, telecommunication, mineral
56 extraction, and pollution from land based activities (Halpern et al., 2019; Amoroso et al., 2018;
57 Keil, 2017). The quantification and mapping of organic carbon on continental margins is therefore
58 imperative for best practise seabed management; with the densities and accumulation rates being
59 a major indicator of ecological function, geological history and ecosystem service provision
60 (Legge et al., 2020; Snelgrove et al., 2018; Middelburg, 2018).

61 In the marine environment, organic carbon can originate from the fixation of carbon dioxide (CO₂)
62 by primary producers in the photic zone or via lateral transport from terrestrial sources (LaRowe
63 et al., 2020b). Organic carbon then passes through a variety of biotic and abiotic pathways being
64 consumed, transformed, respired or remineralised, with a large proportion converted back into
65 inorganic compounds, leaving only ~5% of marine production and less than 1% of earth's gross
66 production eventually reaching the seafloor (Middelburg, 2019; Hülse et al., 2017; Turner, 2015;
67 Bauer et al., 2013; Burdige, 2007). Once at the seafloor, a similarly complex process occurs on
68 and within the sediment, with a wide range of biotic, biochemical and physical processes all
69 influencing the rates of accumulation, remineralisation and resultant long term burial, with ~90%
70 of all carbon reaching the seafloor being remineralised (LaRowe et al., 2020b; Middelburg, 2018,
71 2019; Arndt et al., 2013). Even when considering this complex carbon cycle, the mass and
72 accumulation of organic carbon in surficial seabed sediments will still have a direct influence on
73 the scale of long-term carbon storage at the seafloor (LaRowe et al., 2020a; Middelburg, 2018).

74 Marine habitats are being increasingly recognised as contributors to nature-based climate change
75 mitigation (also known as nature-based climate solutions and natural climate solutions) due to
76 their ability to both fix CO₂ and store organic carbon for centennial to millennial timescales
77 (Macreadie et al., 2021; Hoegh-Guldberg et al., 2019). This "blue carbon" potential was initially
78 recognised in coastal vegetated habitats (i.e. mangrove, seagrass and saltmarsh) (Nellemann et
79 al., 2009; Duarte et al., 2005), but has more recently been applied to other habitats such as kelp
80 forests and unvegetated sediments (Luisetti et al., 2020; Raven, 2018; Avelar et al., 2017). There



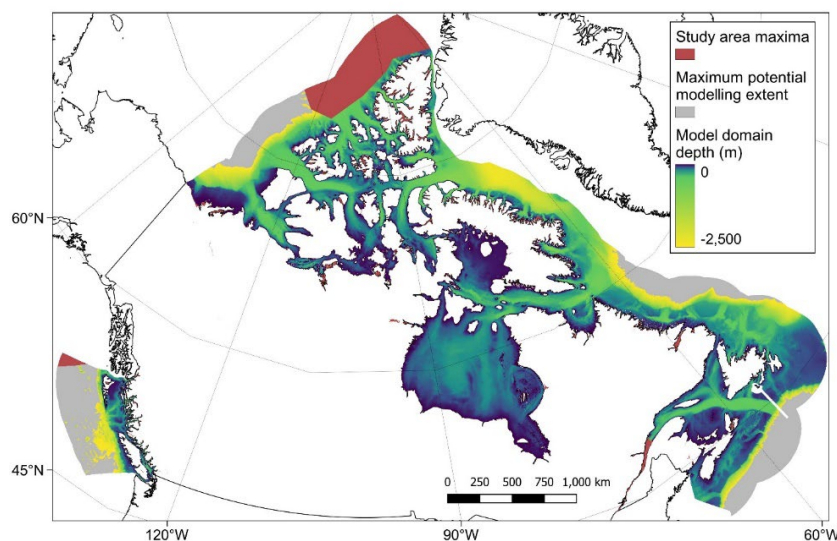
81 is increasing evidence that human activities are influencing seabed sediment carbon stores from
82 both perturbations of upstream processes and physical impacts directly on the seafloor (Cavan
83 and Hill, 2022; Epstein et al., 2022; Keil, 2017; Bauer et al., 2013). For example, a recent study
84 estimated that the direct physical impacts from global fishing activities could cause considerable
85 remineralisation of seabed sediment organic carbon stocks back to CO₂ (Sala et al., 2021),
86 however the validity of the scale of these estimates has been called into question (Hiddink et al.,
87 2023; Hilborn and Kaiser, 2022; Epstein et al., 2022). By improving the accuracy in available
88 sediment carbon mapping products, there may be potential to better research and design
89 appropriate management strategies to enhance organic carbon accumulation or limit
90 remineralisation from disturbance (Epstein and Roberts, 2022; Sala et al., 2021; Luisetti et al.,
91 2019).

92 Historically, studies measuring seabed sediment carbon stocks and accumulation rates had small
93 geographic scope, largely considering the ecological function, geological characteristics or
94 biochemical functioning at local to regional scales (see citations within LaRowe et al., 2020b;
95 Snelgrove et al., 2018; Middelburg, 2018; Burdige, 2007). In recent years, made possible by
96 modern machine learning and statistical spatial prediction techniques, there has been increasing
97 interest in estimating the size and distribution of carbon standing stocks and accumulation rates
98 at national to global scales to better understand natural carbon cycles and biological productivity,
99 and to identify the potential for improved management as a natural climate mitigation strategy
100 (Restrepo et al., 2021; Smeaton et al., 2021; Diesing et al., 2021; Atwood et al., 2020; LaRowe
101 et al., 2020b; Lee et al., 2019; Wilson et al., 2018; Avelar et al., 2017). Although global mapping
102 products can appear to give a complete understanding of seabed sediment organic carbon stocks,
103 there is high inherent uncertainty when making estimates at this scale (Ludwig et al., 2023;
104 Atwood et al., 2020; Lee et al., 2019). This has been highlighted by several regional studies across
105 the northwest European shelf (Smeaton et al., 2021; Diesing et al., 2017, 2021; Luisetti et al.,
106 2020; Wilson et al., 2018), which show distinct spatial patterns in organic carbon distribution and
107 disparate estimates of total standing stocks when compared with these global studies.

108 Canada has the world's longest coastline and approximately the seventh largest Exclusive
109 Economic Zone (EEZ) (Fig. 1), it could therefore be expected to contain a significant proportion
110 of the global stock of seabed sediment organic carbon. Data from recent global studies estimated
111 that the Canadian EEZ contains approximately 2.2 Gt of organic carbon in the top 5 cm and 48
112 Gt in the top meter of seabed sediments, equivalent to ~2.3% of total global marine sediment
113 carbon stocks covering around 1.3% of the area (Atwood et al., 2020; Lee et al., 2019). However,



114 these modelled estimates from global studies are at coarse spatial resolutions, have incomplete
115 coverage and contain very limited *in-situ* data from within the Canadian EEZ itself. The Canadian
116 marine environment is extremely complex, covering three oceans, 46 degrees of latitude, 94
117 degrees of longitude, and containing numerous features including the largest enclosed marine
118 bay in the world, over 50,000 islands, and on the comparatively short Pacific coastline alone,
119 around 436 estuaries. It is therefore highly likely that global estimates of the distribution of seabed
120 sediment organic carbon stock and accumulation rates are inaccurate for this region, and a
121 national approach is needed. Here, we conduct a systematic review of data on seabed sediment
122 organic carbon content across Canada and combine this with a synthesis and unification of best
123 available data on sediment composition, seafloor morphology, hydrology, chemistry and sediment
124 mass accumulation rates in a machine learning predictive mapping process, to construct the first
125 national assessment of Canadian seabed sediment organic carbon stocks and accumulation
126 rates.



127
128 **Figure 1. Map of the Canadian Exclusive Economic Zone (EEZ).** The study area spatial maxima (red; see high
129 resolution figure for further detail around the coastline) covers the entire sub-tidal portion of the Canadian EEZ. This is
130 overlaid by the maximum potential modelling extent (grey) which only includes those areas where data were present
131 for all predictor variables. Due to the distribution of available data, the final model domain was limited to a depth of
132 2,500 meters, and is indicated with the colour relative to the estimated depth, from 0 (dark blue) to -2,500 (yellow).
133 Country outlines from World Bank Official Boundaries, available at
134 <https://datacatalog.worldbank.org/search/dataset/0038272>.

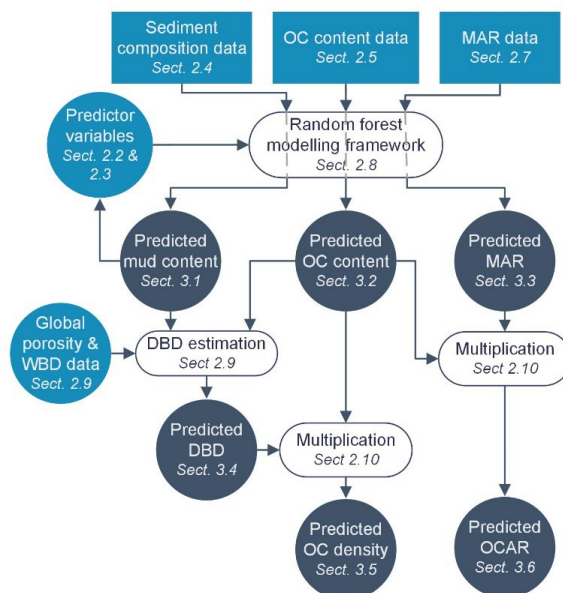
135



136 2. Methods

137 2.1 Analysis software

138 Analyses were primarily undertaken in R 4.2.2 (R Core Team, 2022) and RStudio 2022.12.0.353
139 (Posit Team, 2022), with some additional data manipulation and spatial plotting in QGIS
140 (QGIS.org, 2021) and Python (Van Rossum and Drake, 2009). Within R, raster data were handled
141 using the *terra* package (Hijmans, 2022), spatial vector data using the *sf* package (Pebesma,
142 2018), netCDF data with the *stars* (Pebesma, 2022) and *tidync* (Sumner, 2022) packages, data-
143 frames with the *dplyr* package (Wickham et al., 2019), and vector data with base R (R Core Team,
144 2022). Random forest modelling was primarily dependent on the *ranger* package (Wright and
145 Ziegler, 2017), however models were constructed and tuned using the *tidymodels* package (Kuhn
146 and Wickham, 2020), with cross-validation and predictor variable selection using the *CAST*
147 (Meyer et al., 2023) and *caret* (Kuhn, 2022) packages. Plotting utilised the above packages as
148 well as *ggplot2* (Wickham et al., 2019) and *patchwork* (Pedersen, 2022) while parallel processing
149 used the *doParallel* package (Microsoft Corporation and Weston, 2022). To aid clarity, a workflow
150 diagram of the proceeding methods and results sections is shown in Figure 2.



151

152 **Figure 2. Study workflow diagram.** Outline of the structure and linkages within the proceeding methods and results
153 sections. Light blue shapes indicate input data; white ovals indicate data processes; dark shapes indicate output data;
154 rectangles indicate point data; circles indicate raster data. OC = organic carbon; MAR = mass accumulation rate; WBD
155 = wet bulk density; DBD = dry bulk density; OCAR = organic carbon accumulation rate.



156 **2.2 Study area spatial maxima**

157 To define the maximum potential spatial coverage of this study, best available bathymetric
158 datasets were combined across the Canadian Exclusive Economic Zone (EEZ) (Table 1). Firstly,
159 three Digital Elevation Model (DEM) raster layers covering different extents of the Canadian EEZ
160 were each filtered to contain only those elevations of less than or equal to 0 m. Where necessary,
161 data were then aggregated (averaged) or disaggregated (split) to a resolution of approximately
162 200 m, and all layers were projected onto a unified 200 m x 200 m equal area grid (co-ordinate
163 reference system (CRS) EPSG:3573 - WGS 84 - North Pole Lambert Azimuthal Equal Area
164 Canada). Reprojection was necessary as all three DEMs were in different co-ordinate systems,
165 including some already being projected. The 200 m resolution was chosen as it is the median
166 native resolution of the three DEMs, while also being considered towards the upper limit of what
167 may be computationally possible within the scope of this study. After reprojection, the three layers
168 were overlain, with the region-specific data given priority over global data where present. Finally,
169 the seaward boundaries were delineated by the outer extent of the Canadian EEZ (Flanders
170 Marine Institute, 2019). The resultant bathymetric layer was defined as the study area spatial
171 maxima and used as the first potential predictor variable in predictive modelling (Fig. 1 – covering
172 all coloured areas; Table 1).



173 **Table 1. Summary of predictor variables constructed for the Canadian EEZ.** For more information on methods
 174 used to derive these layers see Sections 2.1 and 2.2.

Predictor variable	Unit	Region	Source	Native resolution	Temporal range
Bathymetry	m	BC	NRCan (2021)	10 m	NA
		Arctic	IBCAO V4.2 (Jakobsson et al., 2020)	200 m	NA
		Global	GEBCO (2022)	0.0042°	NA
Slope	°	Canada	This study	200 m	NA
Slope smoothed	°	Canada	This study	1 km	NA
Total curvature	rad/m	Canada	This study	200 m	NA
Total curvature smoothed	rad/m	Canada	This study	1 km	NA
BPI – fine	m	Canada	This study	200 m	NA
BPI - medium	m	Canada	This study	400 m	NA
BPI - broad	m	Canada	This study	400 m	NA
VRM – fine	-	Canada	This study	200 m	NA
VRM - medium	-	Canada	This study	200 m	NA
VRM - broad	-	Canada	This study	400 m	NA
Distance to shore	m	Canada	This study	200 m	NA
Bioregion	-	Canada	DFO (2022)	NA	NA
Distance to rivers - large	m	Canada	NRCan (2019)	1:15000000	NA
Distance to rivers - medium	m	Canada	NRCan (2019)	1:5000000	NA
Distance to rivers - small	m	Canada	NRCan (2019)	1:1000000	NA
Exposure proxy	-	Canada	This study	200 m	NA
SPM (surface)	g/m ³	Global	Copernicus (2022b)	4 km	2007 - 2019
Wave velocity (seafloor)	m/s	Arctic	Copernicus (2022a)	3 km	2007 - 2019
		Global	Copernicus (2022c)	0.2°	2007 - 2019
Mean current velocity (seafloor)	m/s	BC	Peña et al. (2019)	3 km	2007 - 2019
		Salish Sea	SalishSeaCast ERDDAP v19-05*	500 m	2007 - 2019
		Arctic & Atlantic	ANHA12 (Hu et al., 2019) [†]	0.0833°	2007 - 2019
Temperature (seafloor)	°C	BC	Peña et al. (2019)	3 km	2007 - 2019
		Salish Sea	SalishSeaCast ERDDAP v19-05*	500 m	2007 - 2019
		Arctic & Atlantic	ANHA12 (Hu et al., 2019) [†]	0.0833°	2007 - 2019
Salinity (seafloor)	ppt	BC	Peña et al. (2019)	3 km	2007 - 2019
		Salish Sea	SalishSeaCast ERDDAP v19-05*	500 m	2007 - 2019
		Arctic & Atlantic	ANHA12 (Hu et al., 2019) [†]	0.0833°	2007 - 2019
Ice thickness (surface)	m	Arctic & Atlantic	ANHA12 (Hu et al., 2019) [†]	0.0833°	2007 - 2019
Ice concentration (surface)	%	Arctic & Atlantic	ANHA12 (Hu et al., 2019) [†]	0.0833°	2007 - 2019
Dissolved oxygen (seafloor)	mol/m ³	Global	Bio-ORACLE V2.2 (Assis et al., 2018)	0.0833°	2000 - 2014
Primary production (surface)	g/m ³ /d	Global	Bio-ORACLE V2.2 (Assis et al., 2018)	0.0833°	2000 - 2014
Chlorophyll concentration (surface)	mg/m ³	Global	Bio-ORACLE V2.2 (Assis et al., 2018)	0.0833°	2000 - 2014
Max current velocity (seafloor)	m/s	Global	Bio-ORACLE V2.2 (Assis et al., 2018)	0.0833°	2000 - 2014

175 Notes: BC = British Columbia; BPI = Benthic position index; VRM = Vector ruggedness measure; SPM = Suspended
 176 particulate matter. *See <https://salishsea.eos.ubc.ca/erddap/index.html>; Soontiens and Allen (2017); Soontiens et al.
 177 (2016). [†]See: [https://canadian-nemo-ocean-modelling-forum-community-of-](https://canadian-nemo-ocean-modelling-forum-community-of-practice.readthedocs.io/en/latest/Institutions/UofA/Configurations/ANHA12/index.html)
 178 [practice.readthedocs.io/en/latest/Institutions/UofA/Configurations/ANHA12/index.html](https://canadian-nemo-ocean-modelling-forum-community-of-practice.readthedocs.io/en/latest/Institutions/UofA/Configurations/ANHA12/index.html)

179

180



181 **2.3 Predictor variables**

182 2.3.1 Benthic terrain features

183 A set of 10 benthic terrain features were constructed from the unified bathymetric layer (Table 1).
184 As benthic terrain measures use data on the depth of a location relative to the depth of
185 surrounding cells up to a given distance, bathymetric data within a given buffer outside the study
186 area maxima were included as needed to avoid edge effects in each terrain feature. Slope and
187 total curvature were calculated using the *terra.terrain* (Hijmans, 2022) and *spatialEco.curvature*
188 (Evans and Murphy, 2021) functions respectively. As these measures can be particularly sensitive
189 to artifacts from the DEM models and projections, they were constructed at two resolutions – the
190 native 200 m resolution, and after aggregating the bathymetry by 5-fold to 1 km x 1 km (termed
191 “smoothed”). Smoothed layers were disaggregated back to a 200 m resolution to maintain
192 uniformity across predictor layers.

193 Benthic position index (BPI) and vector ruggedness measures (VRM) were each calculated using
194 the *MultiscaleDTM* package at 3 different levels to capture both small local features and larger
195 spatial variation in terrain (Ilich et al., 2021). Benthic position index was calculated as the
196 difference between the depth of a focal cell and the mean of cells contained in annulus shaped
197 window of 0.2 km to 5 km (BPI fine), 2 km to 25 km (BPI medium) and 4 km to 100 km (BPI broad).
198 Vector ruggedness was measured by considering variation in the depth surrounding each cell
199 within square windows of width 1 km (VRM fine), 5.8 km (VRM medium) and 11.6 km (VRM
200 broad). Due to extremely prohibitive computational times when calculating VRM broad, BPI medium
201 and BPI broad at 200 m resolution, for these features the bathymetric layer was first aggregated
202 to a 400 m resolution before feature calculation, and then disaggregated back to 200 m to
203 maintain uniformity.

204

205 2.3.2 Predictors describing the geographic setting

206 The geographic setting of each cell was described by its distance to shore and rivers, its broad
207 bioregional classification, and a proxy measure describing the degree of exposition vs.
208 shelteredness (Table 1). The geographic setting features are also influenced by the values of
209 surrounding pixels, therefore appropriate buffers were also applied to the processing of these
210 layers to avoid edge effects. Distance to shore was measured by the Euclidian distance to the
211 nearest land cell (indicated by an ‘NA’ value in the bathymetry layer), while bioregion was defined



212 by the Fisheries and Oceans Canada Federal Marine Bioregions classification (DFO, 2022). The
213 bioregion polygons were edited to include all bathymetry cells and re-classified with an integer
214 scale of 1 to 12 from east to west.

215 CanVec is a digital cartographic reference product produced by Natural Resources Canada
216 (NRCan) which includes the location of rivers across Canada at three mapped scales (NRCan,
217 2019). Firstly, the coarsest scale data (1:15,000,000) was projected onto the CRS of the
218 bathymetry layer and converted from polylines to a 2 km resolution raster. A 2 km buffer was
219 added around each river to ensure overlap of river mouths with the bathymetry data. The resultant
220 raster layer was resampled onto the bathymetry raster and the grid distance of each bathymetry
221 cell to the nearest river-mouth cell was calculated using the *terra.gridDist* function (Hijmans,
222 2022). This was then repeated for the medium scale (1:5,000,000) and fine scale (1:1,000,000)
223 layers with each river raster overlaid with the previous coarser scale layer to ensure all rivers
224 were included as the scales decreased.

225 To approximate the exposure setting of each cell, data on the mean distance from shore of
226 surrounding cells was used to construct a proxy value of fetch. Using the *terra.focal* function
227 (Hijmans, 2022), the mean distance to shore of surrounding pixels was calculated in square
228 windows of width 10 km, 20 km, 50 km, 100 km, 175 km and 250 km. Due to extremely inhibitive
229 computational times when calculating these values at the two largest distances, the distance to
230 shore layer was first aggregated to a 400 m resolution before focal calculations of these
231 components, and then disaggregated back to 200 m to maintain uniformity. The maximum value
232 in each layer was then set to the relative window size, and all data in each layer normalised
233 between 0 and 1. The mean of all layers was then calculated which resulted in continuous
234 measure of relative exposure/shelteredness ranging from 0 (highly sheltered) to 1 (highly
235 exposed).

236

237 2.3.3 Satellite derived predictors

238 Using data from the Copernicus Marine Data Store, two layers were created approximating the
239 mass of suspended particulate matter in surface waters and the orbital velocity of waves at the
240 seafloor. Data on suspended particulate matter in surface waters across Canada from 2007 to
241 2019 was extracted in netCDF format from ACRI-ST (Sophia Antipolis, France) company's global
242 Bio-Geo-Chemical products at 4 km spatial resolution and a monthly temporal resolution
243 (Copernicus, 2022b). The climatological mean across this entire period was then calculated for



244 each cell and the netCDF converted to a raster for further processing. Due to the complex nature
245 of the Canadian coastline and the large dissimilarity in spatial resolution of the satellite data
246 product (4 km) and the layers created above (200 m), the satellite raster layer was allowed to
247 extrapolate by 1 cell in its native resolution by taking the mean value of neighbouring pixels. This
248 allowed better overlap of satellite layers with the study area maxima at the coastline but limited
249 over-extrapolation. The raster layer was then reprojected to the equal area CRS and resampled
250 onto the bathymetry layer using cubic-spline interpolation. Due to a lack of consistent SPM data
251 recorded in the northern Arctic Basin, this portion of the data layer was manually removed within
252 QGIS.

253 To calculate the estimated orbital velocity of waves at the seafloor, two satellite wave data
254 products were combined with the unified bathymetry layer as constructed above. Hourly data from
255 2007 to 2019 on the significant wave height (H_s ; VHM0) in meters, and primary wave swell mean
256 period (T_z ; VTM01_SW1) in seconds, were extracted from the 0.2° resolution Global Ocean Wave
257 Reanalysis (WAVERYs) produced by Mercator Océan International (Copernicus, 2022c) and the
258 3 km resolution Arctic Ocean Wave Hindcast produced by MET Norway (Copernicus, 2022a). All
259 data were processed as the SPM data layer (except for lack of removal of the Arctic basin data),
260 and converted to an estimate of orbital wave velocity at the seafloor (U_{rms} ; measured in $m\ s^{-1}$)
261 using the following equation from Soulsby (2006);

$$262 \quad U_{rms} = \left(\frac{H_s}{4}\right) \left(\frac{g}{d}\right)^{0.5} \exp\left\{-\left[\left(\frac{3.65}{T_z}\right) \left(\frac{d}{g}\right)^{0.5}\right]^{2.1}\right\} \quad (1)$$

263 where g is the acceleration due to gravity ($9.806\ m/s^2$) and d is the water depth (m), taken as the
264 unified bathymetry layer multiplied by -1, and all values less than 1 meter depth rounded up to
265 the nearest meter (as needed for the above calculation). The resultant Arctic orbital velocity data
266 layer was then bias corrected to the global orbital velocity data layer utilising the *qmap* package
267 with quantile mapping using a smoothing spline (Gudmundsson et al., 2012). Finally, the two data
268 layers were overlaid with the regional Arctic data taking priority over the global data where
269 available.

270

271 2.3.4 Ocean circulation model predictors

272 Data on the mean surface ice cover, seafloor salinity, temperature and current velocity was
273 collated from three different ocean circulation model products covering different regions of
274 Canada (Table 1). ANHA12 is a regional configuration of the NEMO ocean and sea-ice model



275 (Madec et al., 1998) created at the University of Alberta, covering the Arctic and northern
276 Hemisphere Atlantic at 5 day temporal resolution, a curvilinear 1/12th degree horizontal resolution
277 ranging from 1.93 km in the Arctic to 9.3 km at the equator, and 50 vertical levels (Hu et al., 2019).
278 The British Columbia continental margin (BCCM) circulation model created by Fisheries and
279 Oceans Canada (DFO) covers the entire Canadian Pacific coast and extends approximately
280 400 km offshore. It has a uniform horizontal resolution of 3 km, 42 vertical levels and a 3 day
281 temporal resolution (Peña et al., 2019; Masson and Fine, 2012). As the BCCM model has higher
282 uncertainty in nearshore and enclosed environments due to its relatively coarse resolution, data
283 was also extracted from the Salish Sea Cast ERDDAP data server. Similarly to the ANHA12
284 model, the Salish Sea Cast is a configuration of the NEMO circulation model developed by a
285 consortium of Canadian Universities and government agencies and extends from Juan de Fuca
286 Strait to Puget Sound to Johnstone Strait at 500 m horizontal resolution, 40 vertical layers and
287 hourly temporal resolution (Soontiens and Allen, 2017; Soontiens et al., 2016). For further details
288 on all these models, see relevant cited references. It should be noted that many of these ocean
289 circulation models contain high uncertainty in nearshore areas. However, they are expected to be
290 greatly improved when compared to global circulation model products which are frequently used
291 in this sort of predictive mapping work (e.g. Atwood et al., 2020; Lee et al., 2019; Assis et al.,
292 2018).

293 Three-dimensional data for salinity, temperature, u-velocity (eastward) and v-velocity (northward)
294 was extracted from each model and the climatological mean across all time points between 2007-
295 2019 was calculated. For each horizontal cell, the seafloor value was taken as the lowest vertical
296 cell within a given position. Individual model outputs were then converted to spatial point data
297 using the cell centroid positions and transformed to the unified equal area CRS. Point data was
298 then converted to rasters with the respective resolution of each model, and the mean value taken
299 if two points from the same model lay within a single raster cell as an artifact of reprojection. As
300 the ANHA12 model has a varying horizontal resolution, point data were rasterized using the
301 smallest resolution of the original model (1.6 km) and then interpolated using the *gstat* package
302 (Gräler et al., 2016) and a nearest neighbour interpolation method (including cells for land within
303 the original model grid to suppress extrapolation). For all three models, mean current velocity was
304 then calculated as the root mean square of the u-velocity and v-velocity values in each cell.
305 Finally, as carried out for the satellite data layers, each raster was allowed to extrapolate by one
306 cell in its native resolution (or for the case of the ANHA12 model - its median resolution) and
307 resampled onto the 200 m bathymetry grid using cubic-spline interpolation. The three rasters were
308 then combined; the Salish Sea Cast data only being applied to cells that lay within the Salish Sea



309 bioregion (as calculated in Section 2.3.2), the BCCM model outputs only being assigned to other
310 bioregions within the Pacific and ANHA12 used for all Atlantic and Arctic regions. Although this
311 means that different model products were used to measure the same predictor variable in different
312 regions, which can create biases, the bioregion predictor variable was included as a co-variate in
313 all models which included the ocean circulation variables, thus allowing for interactive effects and
314 accounting for differences in circulation model structures.

315 Predictor layers describing the mean concentration and thickness of sea ice for the same temporal
316 period across the Arctic and Atlantic were also derived from the ANHA12 model. Processing of
317 model data and spatial rasters was conducted as above, except a value of zero ice concentration
318 and thickness was applied to all cells across the British Columbia Pacific bioregions.

319

320 2.3.5 Global model predictors

321 Four additional predictor variables were derived from Bio-ORACLE version 2.2 - a global unified
322 marine environmental data-layers collation which gives climatological mean values at 1/12th
323 degree resolution, for 2000-2014 and a wide-range of environmental variables (Assis et al., 2018).
324 Although these datasets are expected to be of lower accuracy when compared to the regional
325 data used above, based on previous research there were some additional variables not available
326 from the regional circulation models which were considered potentially important for carbon
327 modelling (Diesing et al., 2021; Atwood et al., 2020). Three described the oceanographic
328 chemistry/biology – namely primary production and chlorophyll content of the surface water
329 column, and dissolved oxygen concentration at the seafloor. The fourth predictor was an
330 additional measure of current velocity (maximum current velocity), which was selected on top of
331 the previously derived mean values because current velocity has been identified as a particularly
332 strong predictor within previous seafloor sediment composition and carbon content predictive
333 mapping studies (Grega et al., 2021; Diesing et al., 2021; Mitchell et al., 2019). Raster data were
334 downloaded from the Bio-ORACLE website and processed as the satellite data layers.

335

336 2.3.6 Final collation of predictor variables

337 The resulting 28 predictor variable raster layers were combined into a single raster stack and any
338 cells containing NA values removed, leaving only those cells which contained values across all
339 predictor layers. The remaining cells covered 92.3% of the subtidal zone of the Canadian EEZ



340 and delineated the maximum potential modelling area (Fig. 1). The final predictor variable layers
341 are shown in the Supplement.

342

343 **2.4 Sediment composition data**

344 Sediment composition point data were extracted from two sources. Firstly, all data were exported
345 from the NRCan Expedition Database on 11th November 2022. This data repository contains
346 information related to marine and coastal field surveys conducted by or on behalf of the Geological
347 Survey of Canada from the 1950s to present, which deployed sampling methods including piston
348 cores and grab samples. Data were also extracted from a recent synthesis of grain size
349 distribution measurements from the Canadian Pacific seafloor (1951-2017), compiled by
350 Geological Survey Of Canada and NRCan (Enkin, 2023). Although there are some duplications
351 between these two datasets, these are accounted for in the proceeding pre-processing steps. In
352 both sources, grain size data is reported as the percentage content of mud (sometimes separated
353 into silt and clay), sand and gravel within each sample. Due to modern developments in grain size
354 analyses (e.g. laser diffraction) older samples may have lower measurement accuracy; however,
355 due to the relatively coarse metric being used in this study (%mud/sand/gravel) and the
356 occurrence of a number of largescale geological surveys occurring during the 1960s, we chose
357 to retain data from 1960 onwards. Where sampling year was not recorded within the database,
358 the date was inferred from the expedition code or from expedition metadata. The sampling method
359 and depth of the sediment from which the sample/sub-sample originates are also predominantly
360 recorded within the database. Where sediment depth was absent, but the sampling method was
361 noted as “grab” or “other”, the penetration depth was assumed to be 10 cm (a commonly assumed
362 penetration of standard sediment sampling devices such as Van Veen Grabs and Day Grabs).
363 Samples were only retained if they originated from within the top 30 cm of the sediment and had
364 associated geographic position information (latitude-longitude co-ordinates; lat-lon). Data were
365 further filtered by excluding those where the sum of mud, sand and gravel was greater than 102%
366 and lower than 98% - to allow for rounding errors but to exclude invalid data. Data were also
367 excluded if samples/sub-samples were not present from at least the top 1 cm to 5 cm below the
368 sediment surface within a given sampling event. After data filtering, the mean percentage of mud
369 was taken across replicates/sub-samples, leaving a single value for each sampling event. We
370 chose to concentrate on sediment mud content as this has previously been identified as the key
371 sediment composition component from a number of related carbon mapping studies (Smeaton et
372 al., 2021; Diesing et al., 2017, 2021; Pace et al., 2021; Wilson et al., 2018). Finally, mud content



373 data were projected onto the CRS of the predictor layers and only retained where overlap
374 occurred. This led to a final dataset of 19,730 samples (Fig. A1).

375

376 **2.5 Organic carbon content data**

377 2.5.1 Organic carbon data collation and extraction

378 Data on the percent organic carbon content within dried surface sediments (%OC) was collected
379 from three different structured searches. Firstly, a systematic literature review was conducted
380 through Web of Science and Scopus. Both searches were conducted on the 21st September 2022.
381 Within Web of Science, its “Core collection” was searched via the field “Topic”, which examines
382 a paper’s title, abstract, author, keywords and “keywords plus”. Within Scopus, the search was
383 run via the field “Title-Abs-Key”, which scans a paper’s title, abstract and keywords. Within both
384 databases the same search string was used:

385 (“organic carbon” OR “organic matter” OR “organic content” OR TOC OR TOM) AND (coast* OR
386 sea* OR ocean* OR estuar* OR marine OR gulf) AND (sediment* OR mud* OR sand* OR clay*
387 OR silt* OR gravel* OR seabed) AND Canad*

388 All articles identified from the searches were exported into a single Zotero library and duplicates
389 removed, leaving 1,581 results. Screening was conducted via a hierarchical process that first
390 assessed the title, then abstract and finally full text. At each stage an article was assessed against
391 the inclusion criteria described below, with those considered relevant or of unclear relevance
392 passing to the next level of assessment.

393 The inclusion criteria were defined as: 1) Study conducted on subtidal seabed sediments (those
394 concerning rock, shale or fauna were not included); 2) Physical samples collected using a seabed
395 sediment sampling device (e.g. cores or grabs - sediment-trap samples were not included); 3)
396 Samples from within the Canadian EEZ; 4) Studies concerning the chemical composition of the
397 sediment; 5) Organic carbon content (%) directly measured after separation of organic and
398 inorganic components (e.g. by acidification). After the title screening stage 242 articles remained,
399 followed by 123 remaining after abstract screening, and a final set of 49 articles left for data
400 extraction after review of the full text. Four additional primary literature papers were added based
401 on expert advice.

402 The second structured search was conducted on the Canadian Federal Science Libraries Network
403 - a repository which contains departmental publications, reports and data sets from seven



404 science-based Canadian government departments. The search was carried out on the 7th
405 November 2022 using the same search string as for the primary literature and querying all fields.
406 The search led to only 178 results and therefore each result was assessed individually against
407 the selection criteria first by their abstract and then by a full text assessment, leading to data
408 extraction from 15 reports. The third search was carried out on the 15th November 2022 using
409 GEOSCAN - the NRCan bibliographic database for scientific publications. As GEOSCAN does
410 not allow search strings containing “AND”, the search was conducted on all fields using only the
411 terms: “organic carbon” OR “TOC” OR “OC”; leading to 655 search results. The metadata of all
412 entries was exported as a text file and further refined using a secondary manual search for the
413 remainder of the search terms listed above within Microsoft Excel. This led to a final set of 233
414 results, 178 which were excluded by screening of the title, and a further 51 excluded by abstract
415 or full text screening, leaving 4 reports for data extraction.

416 In total, these three structured searches of primary literature and government reports led to 72
417 individual entries for data extraction. As well as data on the %OC, metadata extracted included
418 the maximum depth of sample into the sediment (cm), geographic position (lat-lon), sample ID,
419 year of sampling (approximated as publication year where not clearly stated), sampling method
420 (e.g. multicorer, Van Veen grab) and water depth of sample site (where recorded). Data were
421 extracted from data tables or supplementary databases when available, otherwise the
422 PlotDigitizer online application was used to extract data from graphical products. Where possible
423 data were extracted on the %OC in different depth-layer sub-samples through a single core-
424 sample up to 50 cm, otherwise a single mean value was taken.

425 Additional to data collated through the structured searches, %OC data were also extracted from
426 PANGAEA - a global data repository for geographic earth-system data (PANGAEA®, 2022). A
427 data search across all topics was conducted on the 25th October 2022 using the same search
428 terms as for the structured search, except for removal of the term “*Canada*”. The geographic
429 extent of the results was instead delineated using the spatial tool within PANGAEA which allows
430 results to be filtered by the geographic co-ordinates of a square/rectangular extent. Overall, this
431 led to a total of 1,489 potential datasets. All relevant data within these datasets were exported
432 using the Data Warehouse Download tool within Pangaea. Based on expert knowledge, two
433 additional PANGAEA datasets were added to the output from published global %OC data-
434 syntheses (Atwood et al., 2020; Seiter et al., 2004). Lastly, where the date of the sample was not
435 recorded, the sampling year was manually added by further exploring the metadata or cited
436 studies. To align the PANGAEA data with the systematic review data, PANGAEA data points



437 were excluded if: 1) they lacked data on %OC; 2) they lacked metadata on the depth of a sample
438 within the sediment; 3) if the sample originated from greater than 50 cm below the sediment
439 surface; or 4) metadata on the elevation/water depth indicated sampling above the subtidal.
440 Additionally, metadata within PANGAEA were coalesced where necessary (due to different
441 names being given to the same data type), and mean values of %OC taken if replicates were
442 measured within a single sub-sample.

443 All organic carbon data were converted into spatial point data, transformed to the unified equal
444 area CRS and masked by the predictor variable's maximum model area to leave only overlapping
445 data. Additionally, values were only retained from the sampling year 1959 and onwards. The extra
446 year was included when compared to the sediment composition data because there were some
447 widescale surveys undertaken across the Labrador Sea in 1959 which was lacking from any
448 additional %OC datasets. While this large temporal extent may add uncertainty in relation to the
449 quality and uniformity of the response data, similar extents have been used by previous global
450 mapping studies (Atwood et al., 2020; Lee et al., 2019; Seiter et al., 2004) and, 72% of the %OC
451 data within this study were sampled after 1980 and 55% after 2000. The larger temporal extent
452 also allows for the inclusion of a larger frequency and wider spatial extent of data, therefore
453 improving accuracy in spatial predictions. In total our %OC dataset contained 2,518 point-samples
454 (Fig. A2) and 3,308 sub-samples across different depth layers within cores.

455

456 2.5.2 Organic carbon data processing

457 Due to commonly adopted uneven sampling distributions within single core samples (i.e. more
458 sub-samples towards the top of the core), where sub-sample data were present on the %OC in
459 different depth-layers these were converted into weighted cumulative means assuming linear
460 distribution between sub-samples. Additionally, there was large variation in the maximum
461 sediment depth of point-samples, ranging from %OC measures from only the top 1 cm of
462 sediment, to values up to the chosen data extraction limit of 50 cm deep. We chose to standardise
463 all samples to 30 cm depth as only 6% of the point-samples covered sediment depths below this
464 layer and because 30 cm is a commonly suggested carbon stock accounting depth for terrestrial
465 soil and marine sediment habitats in both carbon accrediting methodologies and greenhouse gas
466 inventories (VERRA, 2020; IPPC, 2019).

467 To estimate the cumulative mean of %OC at 30 cm for all individual point-samples, we created a
468 transfer function using a generalised additive mixed model (GAMM) smoothing spline. It is



469 generally expected that the %OC in marine sediments decreases with depth within the seafloor
470 (Middelburg, 2018); we used the collated data above to approximate a mean decay function for
471 this study. Firstly, only those data that contained at least five sub-sampled depth layers were
472 retained for modelling as fitting distributions to those with fewer points would likely be invalid. This
473 left 183 unique samples with 2,640 weighted cumulative mean sub-samples for model
474 construction. Cumulative mean %OC data were arcsin transformed ($\arcsin\{\sqrt{[\%OC/100]}\}$; a
475 commonly adopted transformation for percentage data), and a simple GAMM model applied with
476 sub-sample sediment depth as the fixed factor modelled with a cubic regression spline and
477 sample ID as the random factor. The GAMM model was fitted using the *mgcv* package; a scaled-
478 t distribution family was used for heavy tailed Gaussian-like data, the number of basis dimensions
479 was set to 20 and smoothing parameter estimation was conducted by Restricted Maximum
480 Likelihood (REML) (Wood et al., 2016). Model validation was carried out using visual assessment
481 of diagnostic plots of residuals, as well as observed vs fitted values. Significance of the sampling
482 depth smoothing spline was assessed by an analysis of variance (ANOVA) with a chi-squared
483 test comparing the full GAMM model to a null GAMM model containing only the random factor
484 and the intercept (see Appendix B for results). The difference between estimated deviance
485 explained in the full and null models was also used to approximate the variance explained by the
486 fixed and random factors. To create a transfer function, the cumulative %OC was predicted from
487 the mean fixed effects of the GAMM model at sediment depths from 0 – 30 cm at 0.1 cm intervals.
488 The predictions were then back-transformed to percentage data and the cumulative mean %OC
489 at each depth was converted to an inverse proportion of the mean at 30 cm. Overall, this gave an
490 estimated proportional conversion factor from the cumulative mean at any given depth to an
491 expected cumulative mean at 30 cm (Appendix B).

492 All point-sample data from PANGAEA and the systematic review were combined, corrected to
493 weighted cumulative means where sub-samples were present, checked for duplication, and
494 unified to a mean %OC value of the top 30 cm of sediment using the above transfer function. One
495 outlier was removed from the dataset as it was reported to have a carbon content twice that of
496 any other sample within the dataset. Finally, for further analyses %OC data were arcsin
497 transformed due to a highly right skewed distribution and its application within similar modelling
498 exercises (Smeaton et al., 2021; Diesing et al., 2017).

499

500



501 **2.6 Final model domain selection**

502 After visual assessment of the coverage of both the sediment composition and %OC data, the
503 final model domain was limited to a water depth of 2,500 meters. This depth limit (as delineated
504 by the bathymetry predictor layer) encompassed 99.95% of sediment composition point data (Fig.
505 A1) and 99.3% of %OC data (Fig. A2). The predictor layer raster stack was filtered with all cells
506 deeper than 2,500 meters excluded from the model domain. This final model domain covers
507 4,489,235 km² which is 78.4% of the EEZ or 92.6% of the seafloor area above 2,500 m (Fig. 1).

508

509 **2.7 Sediment mass accumulation rate data**

510 From preliminary exploratory research it was determined that there would be insufficient data on
511 organic carbon accumulation rates, or sediment mass accumulation rates, to undertake a
512 Canada-specific data synthesis. We therefore chose to downscale a recent global spatial
513 predictive map of seafloor sediment mass accumulation rates (Restrepo et al., 2021). To
514 approximate a sample of values across the model domain in this study the global mass
515 accumulation rate data (MAR; $\log_{10}\{\text{g cm}^{-2} \text{ yr}^{-1}\}$) netCDF was converted to a raster and masked
516 by the coverage of the model domain. The raster layer was then converted to spatial point data
517 by the location of cell centroids, and a stratified-random sample of 10% of the data was taken.
518 Data was stratified by assigning the x-coordinate, y-coordinate and mass accumulation rate
519 values to decile bins; and a random sample of 10% of values taken within each unique
520 combination of the three-way binning. This resulted in 12,660 point estimates of MAR across the
521 model domain, which were then reprojected to the unified equal area CRS for further analyses
522 (Fig. A3).

523

524 **2.8 Random forest modelling**

525 For predictive mapping we adopted random forest machine learning techniques due to their
526 flexibility regarding violations of traditional statistical assumptions, ability to handle a range of data
527 types and predictor variables and elucidate both drivers of model response and predictions of
528 uncertainty, as well as their successful application in previous similar modelling tasks (Diesing et
529 al., 2017, 2021; Pace et al., 2021; Atwood et al., 2020; Wilson et al., 2018). Contemporary
530 research in spatial machine learning techniques have highlighted that robust spatially-explicit
531 cross-validation (CV) strategies and predictor variable selection processes are essential to



532 calculate valid performance metrics, limit overfitting and construct reliable spatial predictions
533 (Zhang et al., 2023; Ludwig et al., 2023; Meyer and Pebesma, 2022; Meyer et al., 2019). We
534 discuss the incorporation of these processes into our modelling framework below.

535 Three response variables (mud content, organic carbon content (%OC) and MAR) were modelled
536 using the following framework. Firstly, each response variable was overlain onto the predictor
537 variable grid and the mean values were taken if more than one data-point fell within a single raster
538 cell. All predictor variable data were then extracted for each response dataset; however, the three
539 biological/biochemical predictor variables (primary production, chlorophyll concentration and
540 dissolved oxygen) were only used within the %OC model as they are not expected to drive
541 variation in physical sediment properties (Restrepo et al., 2021; Gregr et al., 2021; Graw et al.,
542 2021; Mitchell et al., 2019).

543 For each response variable, the *spatialsample* package (Silge and Mahoney, 2023) was used to
544 construct a variety of spatial CV data-fold structures (splitting the data into different analysis and
545 assessment sets) and the validity of each structure was visually assessed using the
546 *CAST.plot_geodist* function (Meyer et al., 2023). This function creates density plots of nearest
547 neighbour distances in multivariate predictor space between all response data as well as between
548 response data and a random sample of prediction locations, and between analysis and
549 assessment data within CV folds (see Appendix C). The suitability of a given CV structure to be
550 representative of estimating map accuracy can be determined by visually assessing the density
551 plots and finding the analysis-to-assessment CV-distance curve being closely aligned to the
552 sample-to-prediction density curve (see Appendix C; Ludwig et al., 2023; Meyer and Pebesma,
553 2022). Contrastingly, if the sample-to-sample distance curve closely overlays the sample-to-
554 prediction curve, this indicates that traditional random cross-validation strategies are likely to be
555 appropriate (see Appendix C; Ludwig et al., 2023). To approximate sample-to-prediction
556 distances, the sample size number within *plot_geodist* was set to select 5,000 random samples
557 across the model domain. Further, as the spatial distribution of data is a key consideration to
558 ensure robust cross-validation (Ludwig et al., 2023; Meyer and Pebesma, 2022), the x- and y-
559 coordinates of each data point were also included as predictor variables in the *plot_geodist*
560 calculations.

561 For the mud content data, a spatial kmeans clustering CV structure was chosen as the response
562 data had good coverage of the model domain, contained a large number of data points, and
563 showed relatively strong spatial clustering (Fig. A1). A range of options in the number of kmeans
564 clusters were tested, with 35 being determined as the optimal number and each cluster being



565 assigned to its own CV fold (Fig. C1). Through visual assessment of the density plots, it was
566 identified that the kmeans CV structure was somewhat mis-aligned from response-to-prediction
567 distances, with the CV distances being overly conservative at including near-distance
568 comparisons (Fig. C1). We therefore used a partially repeated CV strategy, with a small number
569 of randomly selected data-points added to the assessment set in each kmeans spatial-CV fold
570 (1% of mud content data randomly sampled at each fold without replacement) (Fig. C2). As the
571 %OC response dataset was relatively small and spatially dispersed (Fig. A2), we used a spatial
572 block CV strategy in place of the kmeans clustering to avoid clusters containing highly spatially
573 dispersed data. We chose to use hexagonal shaped blocks, random assignment of blocks to folds,
574 and the same number of CV folds as for the mud content data ($v = 35$) - both to maintain uniformity
575 and because varying the fold-number did not significantly influence the density plots. Instead, the
576 diameter of the spatial blocks was altered, and an optimal block size of 100 km identified using
577 the *plot_geodist* function (Fig. C3). For both response variables, following identification of an
578 appropriate CV structure, a single fold was assigned as testing data, with all other data retained
579 for model fitting. Following the training-testing split, the spatial CV folds were reconstructed on
580 the training data to ensure an absence of duplication. For the MAR data, the density plots
581 indicated that traditional random cross-validation would be a valid approach (Fig. C4), which was
582 expected as the response data were a stratified-random sample across the model domain (Fig.
583 A3). The random CV folds were stratified by the MAR response value to ensure a relatively even
584 distribution across CV folds. A 10% stratified-random sample was first assigned as the test-set
585 and random CV folds assigned to the remaining training data.

586 Three random forest models were constructed (mud content, OC content and MAR), each
587 following the same modelling protocol. Firstly, the *CAST.ffs* function (Meyer et al., 2023) was used
588 to run a spatially-explicit forward predictor variable selection processes. The function fits a model
589 with all combinations of two-way predictors, selects the best model based on a given metric, and
590 then increases the number of predictors by one, testing all remaining variables. This iteratively
591 continues with the process stopping if none of the tested variables increases the performance
592 when compared to the best previous model with “n-1” predictors. The function also allows models
593 to be fit separately across all individual CV folds, therefore incorporating appropriate spatial
594 considerations into the feature selection process. Due to the large number of variables within this
595 study, and the relatively large datasets, this process was very computationally expensive. We
596 therefore chose to adapt the function to initiate forward variable selection after *a priori*
597 identification of the first two predictor variables. These variables were identified by constructing a
598 basic random forest model with all training data and predictor variables, and the hyperparameters



599 *mtry* (the number of variables to randomly sample as candidates at each split), *min_n* (the number
600 of observations needed to keep splitting nodes) and *trees* (the number of random forest trees to
601 construct and take mean predictions across) set to 2, 5 and 1,000 respectively. Variable
602 importance was estimated using permutation, and the two predictor variables with largest
603 importance selected. The *ffs* function was then run starting with the two pre-selected variables
604 (see Fig. 3, 6 & 9) and performance of each iteration assessed on the root mean squared error
605 (RMSE) of predictions across all CV folds.

606 Following variable selection, hyperparameter tuning was conducted on the *mtry* and *min_n*
607 hyperparameters, with the number of trees set to 1,000. The tuning process fitted individual
608 models across all CV folds, each with 11 combinations of hyperparameters which were selected
609 using a semi-random Latin hypercube grid. The performance of each hyperparameter
610 combination was assessed based on the RMSE of predictions across all CV folds. After selection
611 of the best performing hyperparameter combination, a last model fit was conducted on the entire
612 training set and evaluated on the test set, with the absence of overfitting determined by the RMSE
613 and R^2 of the last-fit model falling within the range of those found across CV folds. Overall model
614 performance metrics (RMSE and R^2) were then calculated using the predictions across all CV
615 folds with optimal hyperparameters and the last-fit; while predictor variable importance was
616 calculated by fitting an additional model across all training data using optimal tuning parameters
617 and the importance calculated through permutation. Accumulated local effects (ALE) plots were
618 produced for the six predictor variables with highest importance in each model using the *iml*
619 package (Molnar et al., 2018) to give a visual representation of the average effect of predictors
620 on model prediction outcomes. Finally, mean model predictions were calculated across the entire
621 model domain using the last-fit model and the predictor variable raster stack, and cell-specific
622 estimation of uncertainty was calculated using standard error on out-of-bag predictions using
623 infinitesimal jack-knife for bagging (Roy and Larocque, 2020; Wager et al., 2014). Due to
624 computational restraints when calculating predictions across the entire model domain (which
625 contains 112,230,871 cells), data were split into 150 random samples (without replacement) and
626 both prediction and standard error estimates made serially on each split. All predictions were then
627 merged to create a raster layer covering the entire model domain.

628 A cell-specific approximation of the upper and lower bounds of the 95% confidence interval (CI)
629 was calculated by adding/subtracting the cell-specific standard error estimates, each multiplied
630 by 1.96, from the mean predictions and then back transformed where needed (Kuhn and
631 Wickham, 2020; Wager et al., 2014). After calculation, CI values were corrected where necessary



632 - being bounded by 0, and where applicable also bounded by 100. The resulting three raster
633 layers from the mud content model were also used as available additional predictor variables
634 when constructing the random forest models for %OC and MAR as outlined above (Fig. 2).

635

636 **2.9 Estimating sediment dry bulk density**

637 To estimate the dry bulk density of the sediment across the model domain (ρ_D – the mass of dried
638 sediment per unit volume within the seafloor; g cm^{-3}) the outputs from the random forest models
639 for mud and organic carbon content were combined with a variety of published transfer functions
640 and global modelled products (Fig. 2). Three of the transfer functions calculate the porosity of the
641 sediment (Φ ; the proportion of sediment volume which is water) based on the predicted mud
642 content using the following equations, respectively from Jenkins (2005), Diesing et al. (2017) and
643 Pace et al. (2021):

$$644 \quad \Phi = 0.3805 \cdot \text{mud} + 0.42071 \quad (2)$$

$$645 \quad \Phi = 0.4013 \cdot \text{mud} + 0.4265 \quad (3)$$

$$646 \quad \Phi = 10^{\{0.138 \cdot \log_{10}(\text{mud}) - 0.486\}} \quad (4)$$

647 In all cases *mud* is the predicted values across the model domain as calculated above expressed
648 as a decimal proportion. For Equation 4 mud content was rounded up to the nearest 0.01 as lower
649 values give unrealistic porosity estimates. All sediment porosity estimates were then converted to
650 an estimate of dry bulk density using the following equation:

$$651 \quad \rho_D = \rho_S(1 - \Phi) \quad (5)$$

652 where ρ_S is the grain density of seabed sediments in g cm^{-3} , which was set at the frequently used
653 constant approximation of 2.65 (Diesing et al., 2017, 2021; e.g. Pace et al., 2021; Lee et al., 2019;
654 Wilson et al., 2018; Kuzyk et al., 2017). Although this standard approximation of grain density is
655 not ideal, the variation under different environmental settings is generally found to be small when
656 compared to differences in %OC and porosity, therefore the values of grain density are not
657 expected to strongly drive variation in organic carbon density (Atwood et al., 2020; Lee et al.,
658 2019; Middelburg, 2019; Martin et al., 2015; Berner, 1982). A fourth transfer function from Atwood
659 et al. (2020) calculates an estimate of dry bulk density directly from %OC using the following
660 equation:

$$661 \quad \rho_D = 0.861 \cdot \%OC^{-0.3999} \quad (6)$$



662 For this equation, carbon content as predicted above was rounded up to the nearest 0.1% as
663 lower values give unrealistic dry bulk density estimates. For each of the four transfer functions
664 (Equations 2,3,4 and 6) the value was calculated using the mean prediction as well as the upper
665 and lower confidence interval bounds of mud content and %OC respectively, resulting in three
666 raster layers from each function.

667 Two further estimates of dry bulk density were calculated using products from global predictive
668 models, both at 5 arc min spatial resolutions. Martin et al. (2015) created a predictive map of
669 seabed sediment porosity, while Graw et al. (2021) estimate sediment wet bulk density (ρ_W)
670 across the global seafloor. Both raster layers were processed as the satellite predictor layers to
671 align with the model domain. The resulting porosity raster layer was converted to dry bulk density
672 using Equation 5, while the wet bulk density layer was initially converted to porosity using the
673 equation:

$$674 \quad \phi = \frac{\rho_W - \rho_S}{\rho_{SW} - \rho_S} \quad (7)$$

675 where ρ_{SW} is the density of seawater estimated as 1.024 g/cm³. In total this led to 14 dry bulk
676 density estimates across the model domain. A final mean value and standard error was calculated
677 for each cell, and the upper and lower 95% confidence interval bounds calculated using the
678 standard error as above.

679

680 **2.10 Estimating organic carbon standing stock and accumulation rates**

681 The organic carbon density (g cm⁻³) is calculated by multiplying the %OC (expressed as a decimal
682 proportion) by the sediment dry bulk density; while organic carbon accumulation rates (g cm⁻² yr
683 ⁻¹) are calculated by multiplying MAR by %OC (Fig. 2). For the final calculations of both density
684 and accumulation the respective means, upper and lower CI bounds were multiplied together to
685 incorporate uncertainty from both components. To create more meaningful response values
686 organic carbon density was converted to kg m⁻³ (multiplied by 1000) and organic carbon
687 accumulation to g m⁻² y⁻¹ (multiplied by 10,000). Finally, the organic carbon stock in each mapped
688 cell can be calculated by multiplying the organic carbon density by the reference sediment depth
689 of this study (0.3 m) and the cell area (40,000 m²) and converted to metric tonnes (divided by
690 1000). The total accumulation per cell per year can be calculated by multiplying the organic carbon
691 accumulation rate by the cell area. Overall, this allows estimates to be calculated for the total
692 values of organic carbon stock and accumulation across different parts of model domain.



693

694 **2.11 Rock substrate distribution case studies**

695 The method followed in this study is similar to that used for many similar predictive mapping
696 exercises in that it uses data only from sediment grab and core samples to build predictive maps
697 across the model domain (Restreppo et al., 2021; Graw et al., 2021; Diesing et al., 2017, 2021;
698 LaRowe et al., 2020a; Atwood et al., 2020; Lee et al., 2019; Mitchell et al., 2019; Wilson et al.,
699 2018; Stephens and Diesing, 2015). One major limitation with this modelling approach is that
700 areas of bedrock, which would have zero values for all sediment response variables, will not be
701 recorded in these datasets. Therefore, the under representation of zero values in the response
702 data could lead to an overestimate of organic carbon standing stocks and accumulation rates as
703 zero values are unlikely to be predicted from model outputs.

704 In the context of this study, information regarding the distribution of bedrock is lacking for many
705 regions. We therefore use two regional case studies from the Pacific British Columbian EEZ and
706 the Atlantic Scotian shelf and slope where recent publications have made estimated maps on the
707 distribution of rock substrates (Philibert et al., 2022; Gregr et al., 2021). Each of these products
708 was overlaid onto the final spatial predictions of sediment carbon densities and accumulation
709 rates and all cells set to zero where rock substrates were predicted. The proportional effect on
710 the mean, upper and lower confidence interval bounds of estimated carbon stock and
711 accumulation rates was then calculated in each bioregion.

712

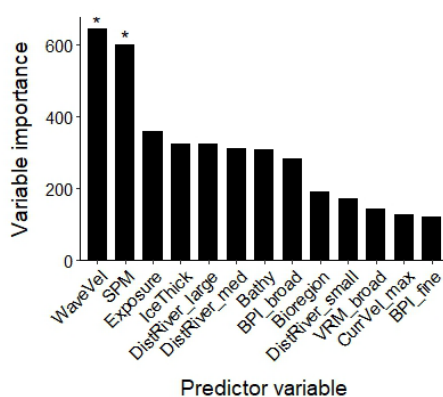
713 **3. Results**

714 **3.1 Mud content predictive mapping**

715 Of the 25 predictor variables available for mud content random forest modelling, 13 were selected
716 in the optimal model (Fig. 3). Mean orbital velocity of waves at the seafloor and the mass of
717 suspended particulate matter at the surface were the variables with highest importance (Fig. 3).
718 Other variables with relatively high importance for predicting mud content included the exposure
719 setting, ice thickness, distance to rivers, bathymetry, and benthic position indices (Fig. 3). Higher
720 mud content was generally predicted in areas of low wave velocity, low exposure and close to but
721 not directly adjacent to river mouths; with the effect of SPM and ice thickness less distinct, likely
722 due to more complex interactive effects (Fig. 4).



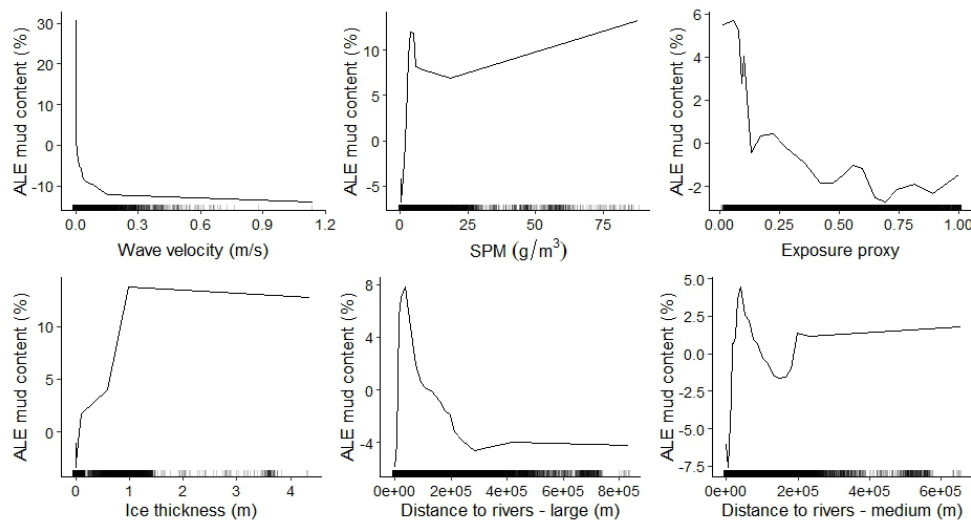
723



724

725 **Figure 3. Predictor variable importance from random forest models of mud content in marine subtidal**
 726 **sediments.** The y-axis is a unitless relative variable importance score for each model. Asterisks indicate the *a priori*
 727 variable selection. WaveVel = Orbital wave velocity at the seafloor, SPM = Suspended particulate matter within the
 728 water column, BPI = Benthic position index, DistRiver = Distance to nearest river, IceThick = Sea ice thickness, Bathy
 729 = Bathymetry, VRM = Vector ruggedness measure, CurrVel = Current velocity at the seafloor.

730



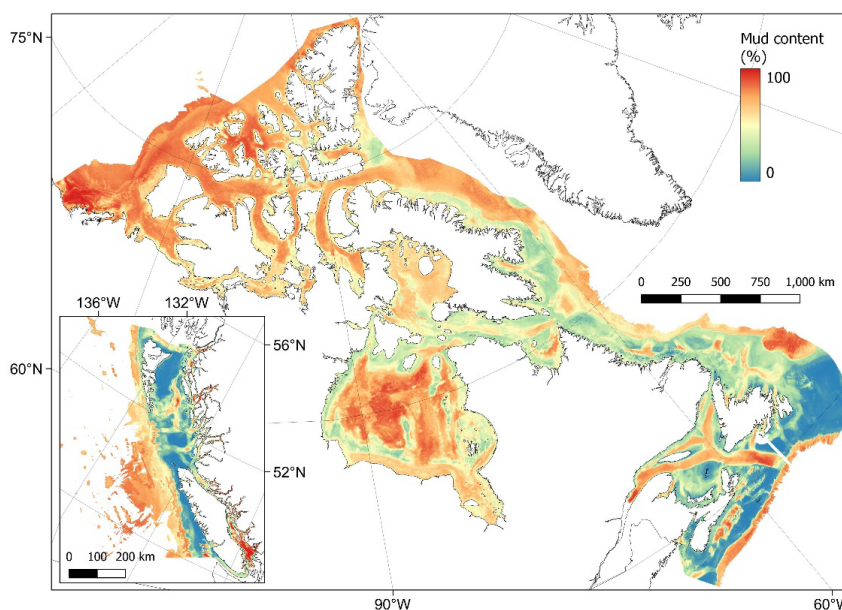
731

732 **Figure 4. Accumulated local effects (ALE) plots for the six predictor variables with highest importance in the**
 733 **mud content random forest model.** ALE gives a visual representation of the average effect of the predictor variable
 734 on the response but does not indicate the influence of multi-way interactions which are inherent in random forest
 735 models. Rug plots indicate the distribution of each variable within the training dataset. SPM = suspended particulate
 736 matter.



737

738 Areas with sediments dominated by mud (>75%) were predicted across the basins of many of the
739 Pacific fjords, inlets and estuaries, and within the southern Salish Sea (Fig. 5). In the Arctic, mud
740 dominated areas included large parts of the Canadian western Arctic as well as Hudson Bay. In
741 the Atlantic, the Laurentian channel and central Scotian Shelf contained particularly high mud
742 fractions (Fig. 5). Across the model domain, sediment in deeper areas on the continental slope
743 was also highly dominated by mud (Fig. 5) Using robust spatial cross validation, the model was
744 estimated to have an RMSE of 24.4% and R^2 of 0.60. The cell specific upper and lower 95% CI
745 bounds are shown in Figure D1. On average the upper CI bounds were 28% higher than the mean
746 and the lower CI bounds 20% less.



747

748 **Figure 5. Predictive mapping of mud content (%) in subtidal marine sediments across the Canadian continental**
749 **margin.** The main plot shows the Arctic and Atlantic regions with the Pacific region inset. The 95% confidence interval
750 bounds around the predicted means are shown in Figure D1. Labels indicating the locations of different areas
751 mentioned within the text are shown in Figure A4. Country outlines from World Bank Official Boundaries, available at
752 <https://datacatalog.worldbank.org/search/dataset/0038272>.

753

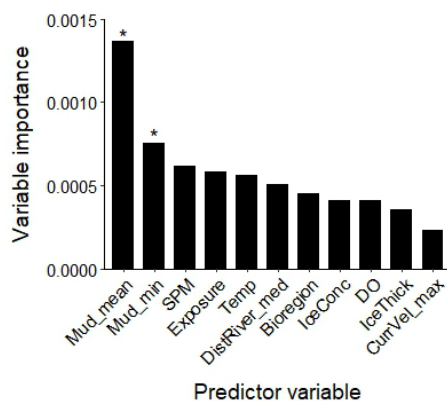
754



755 3.2 Organic carbon content predictive mapping

756 Eleven predictor variables were selected in the optimal organic carbon content (%OC) model (Fig.
757 6). The variables with highest importance in predicting %OC were the mud content layers
758 constructed above (specifically the mean and lower CI bound), with all other predictors having
759 less than half the relative importance of the mean mud predictions (Fig. 6). On average organic
760 carbon content increased with predicted mud content and was generally higher in areas with low
761 SPM concentrations, low exposure settings, close to but not directly adjacent to rivers, and at high
762 water temperatures (Fig. 7).

763



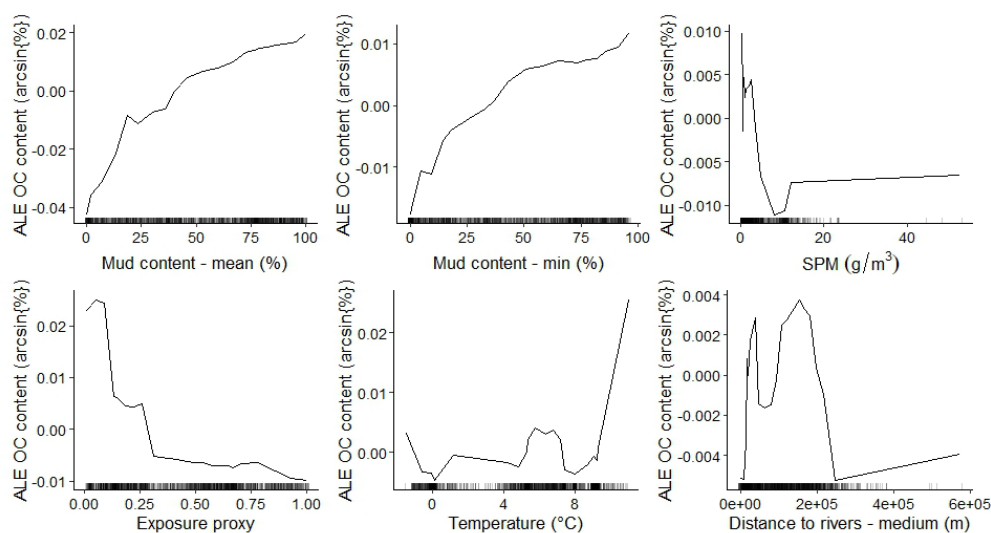
764

765 **Figure 6. Predictor variable importance from random forest models for the organic carbon content in marine**
766 **subtidal sediments.** The y-axis is a unitless relative variable importance score. Asterisks indicate the *a priori* variable
767 selection. Mud_min = Lower bound of 95% CI for mud content, SPM = Suspended particulate matter within the water
768 column, Temp = Temperature, DistRiver = Distance to nearest river, IceConc = Sea ice concentration, DO = Dissolved
769 oxygen at the seafloor, IceThick = Sea ice thickness, CurrVel = Current velocity at the seafloor.

770



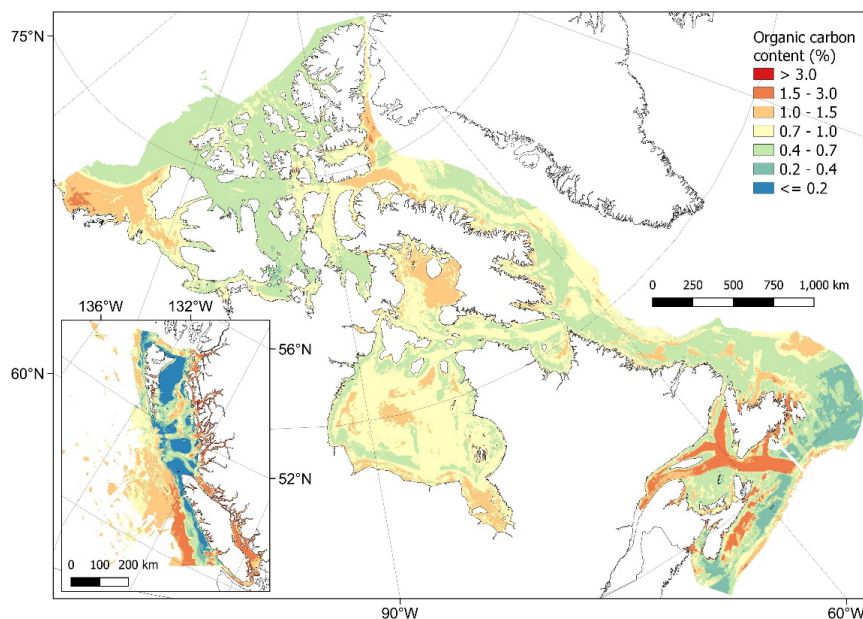
771



772

773 **Figure 7. Accumulated local effects (ALE) plots for the six predictor variables with highest importance in the**
774 **organic carbon (OC) content random forest model.** ALE gives a visual representation of the average effect of the
775 predictor variable on the response but does not indicate the influence of multi-way interactions which are inherent in
776 random forest models. Rug plots indicate the distribution of each variable within the training dataset. SPM = suspended
777 particulate matter.

778 The predictions of %OC ranged from 3×10^{-5} to 5.6% with an overall mean of $0.8 \pm 0.3\%$ (\pm SD).
779 Areas with highest predicted %OC ($>3\%$) were restricted to parts of the Pacific west coast fjords
780 and channels, and in small parts of the inlets and bays on the east coast of Nova Scotia and
781 around Passamaquoddy Bay in the Bay of Fundy (Fig. 8). High concentrations (i.e. $>1\%$) were
782 more widespread across these areas as well as covering much of the Beaufort Sea, western
783 Baffin Bay and Foxe Basin in the Arctic, southern and central Hudson Bay, the Laurentian
784 channel, coastal north Newfoundland and the central Scotian shelf in the Atlantic, as well as
785 across the Salish sea and deeper areas to the south of the British Columbian continental margin
786 (Fig. 8). Lowest %OC was predicted across shallower parts of the central Pacific shelf and near
787 coast areas west of Vancouver Island (Fig. 8). Cross validation estimated an R^2 for the model of
788 0.58 and an RMSE of 0.09 arcsin{%OC}. Cell specific upper and lower 95% CI bounds are shown
789 in Figure D2. On average the upper CI bounds were 42% higher than the mean prediction, and
790 the lower CI bounds 33% less than the mean prediction.

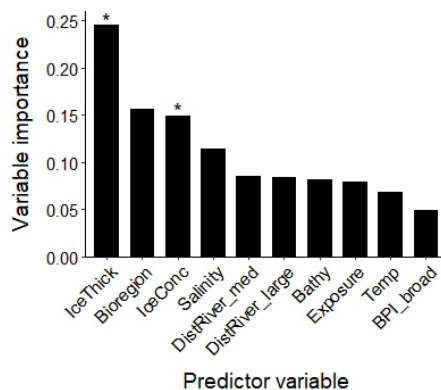


791

792 **Figure 8. Predictive mapping of organic carbon content (%) in subtidal marine sediments across the Canadian**
793 **continental margin.** The main plot shows the Arctic and Atlantic regions with the Pacific region inset. The continuous
794 variable is shown displayed in discrete colour bands to improve visualisation of highly right skewed data. The 95%
795 confidence interval bounds around the predicted means are shown in Figure D2. Labels indicating the locations of
796 different areas mentioned within the text are shown in Figure A4. Country outlines from World Bank Official Boundaries,
797 available at <https://datacatalog.worldbank.org/search/dataset/0038272>.

798 3.3 Sediment mass accumulation rate predictive mapping

799 The optimal model for mass accumulation rate (MAR) of seabed sediments contained 10
800 variables (Fig. 9). On average, MAR was negatively associated with increasing ice thickness, ice
801 concentration, salinity and distance from rivers, and was particularly high in Eastern bioregions
802 (Fig. 10). The predictions of MAR ranged from 4×10^{-4} to $0.35 \text{ g cm}^{-2} \text{ yr}^{-1}$ with an overall mean of
803 $0.01 \pm 0.03 \text{ g cm}^{-2} \text{ yr}^{-1}$ (\pm SD). Areas with highest MAR ($>0.1 \text{ g cm}^{-2} \text{ yr}^{-1}$) were predicted on the
804 east coast around inshore areas of the Gulf of St Lawrence and Bay of Fundy (Fig. 11). Other
805 areas with higher than average MAR were predicted across Canadian inshore areas particularly
806 in the southern Arctic, Hudson Bay, Foxe Basin, Salish Sea and northeast British Columbia Pacific
807 shelf (Fig. 11). The optimal model had an estimated R^2 of 0.89 and RMSE of $0.206 \log_{10}\{\text{g cm}^{-2}$
808 $\text{yr}^{-1}\}$. Cell specific upper and lower 95% CI bounds are shown in Figure D3. On average the upper
809 CI bounds were 33% higher than the mean prediction, and the lower CI bounds 20% less than
810 their means.

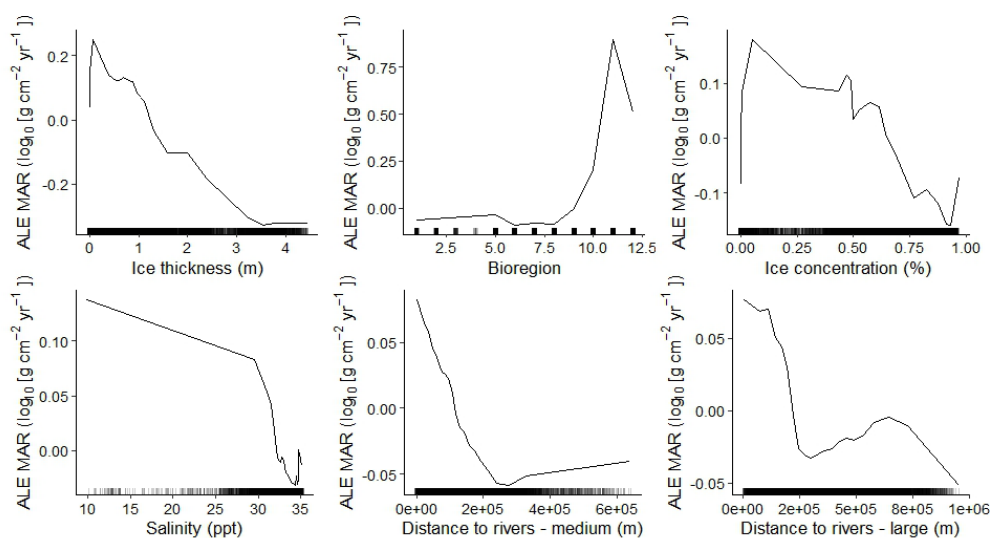


811

812 **Figure 9. Predictor variable importance from random forest models for the mass accumulation rate of subtidal**
 813 **sediments.** The y-axis is a unitless relative variable importance score. Asterisks indicate the *a priori* variable selection.
 814 IceThick = Sea ice thickness, IceConc = Sea ice concentration, DistRiver = Distance to nearest river, Bathy =
 815 Bathymetry, Temp = Temperature, BPI = Benthic position index.

816

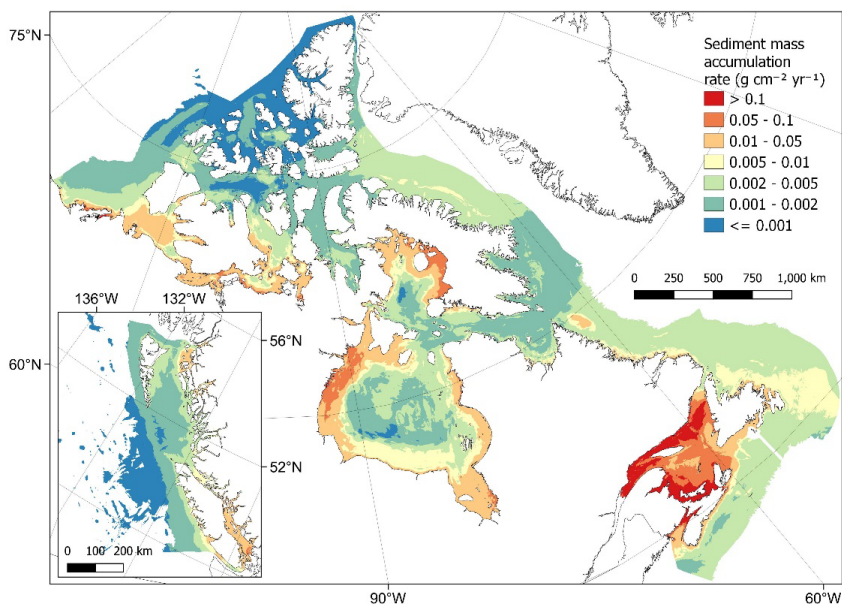
817



818

819 **Figure 10. Accumulated local effects (ALE) plots for the six predictor variables with highest importance in the**
 820 **sediment mass accumulation rate (MAR) random forest model.** ALE gives a visual representation of the average
 821 effect of the predictor variable on the response but does not indicate the influence of multi-way interactions which are
 822 inherent in random forest models. Rug plots indicate the distribution of each variable within the training dataset.

823



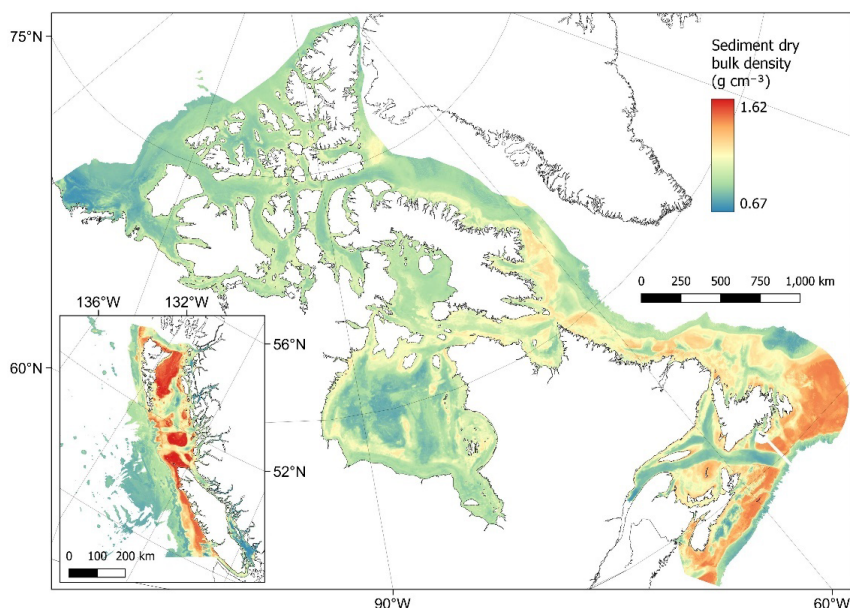
824

825 **Figure 11. Predictive mapping of sediment mass accumulation rate ($\text{g cm}^{-2} \text{yr}^{-1}$) across the Canadian**
826 **continental margin.** The main plot shows the Arctic and Atlantic regions with the Pacific region inset. The continuous
827 variable is shown displayed in discrete colour bands to improve visualisation of highly right skewed data. The 95%
828 confidence interval bounds around the predicted means are shown in Figure D3. Labels indicating the locations of
829 different areas mentioned within the text are shown in Figure A4. Country outlines from World Bank Official Boundaries,
830 available at <https://datacatalog.worldbank.org/search/dataset/0038272>.

831

832 **3.4 Dry bulk density estimation**

833 The dry bulk density of sediments was estimated using a variety of transfer functions and global
834 predictions (Fig. 2). Estimated values ranged from $0.67 - 1.62 \text{ g cm}^{-3}$ with a mean of 1.02 ± 0.16
835 g cm^{-3} (\pm SD). As many of the transfer functions are dependent on the predicted mud content, the
836 spatial distribution of dry bulk density values was very similar to the mud content values predicted
837 above (Fig. 5), i.e. lowest dry bulk density was estimated in mud dominated areas (Fig. 12). Cell
838 specific upper and lower 95% CI bounds are shown in Figure D4. On average CI bounds were
839 8.5% either side of their means.



840

841 **Figure 12. Estimates of sediment dry bulk density (g cm^{-3}) across the Canadian continental margin.** The main
842 plot shows the Arctic and Atlantic regions with the Pacific region inset. The 95% confidence interval bounds around the
843 predicted means are shown in Figure D4. Labels indicating the locations of different areas mentioned within the text
844 are shown in Figure A4. Country outlines from World Bank Official Boundaries, available at
845 <https://datacatalog.worldbank.org/search/dataset/0038272>.

846

847 **3.5 Estimated organic carbon density and standing stock**

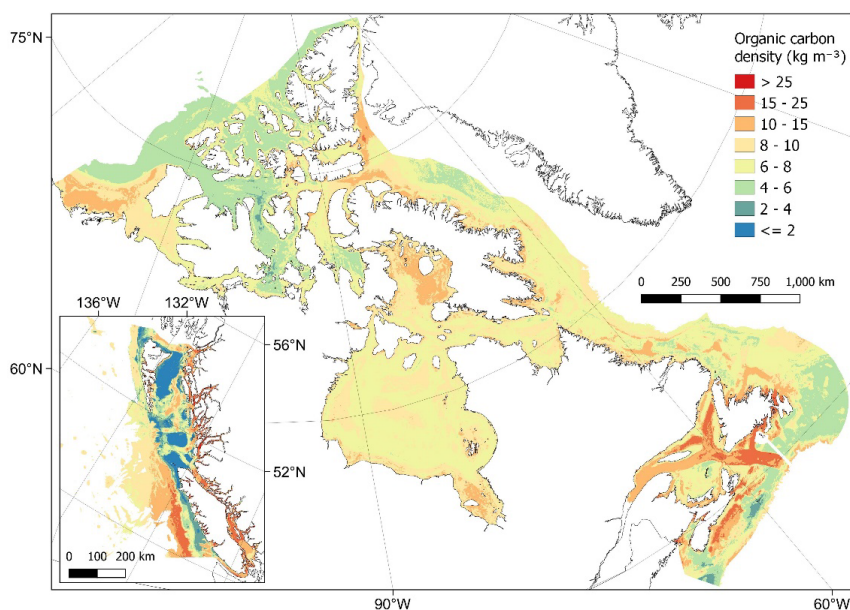
848 From combining predictions of dry bulk density and organic carbon content, organic carbon
849 density could be estimated across the Canadian continental margin (Fig. 2). Estimated values
850 ranged from 5×10^{-4} to 50.0 kg m^{-3} with a mean of $7.9 \pm 2.5 \text{ kg m}^{-3}$ (\pm SD). Spatial patterns in
851 organic carbon density (Fig. 13) were similar to those found for organic carbon content (Fig. 8).
852 Areas with highest carbon density ($> 25 \text{ kg m}^{-3}$) were restricted to small areas within nearshore
853 zones, including inlets and fjords of British Columbia, as well as enclosed nearshore areas of the
854 Atlantic East Coast (Fig. 13). High carbon densities ($> 15 \text{ kg m}^{-3}$) were predicted to occur across
855 wide parts of these areas as well as further offshore in parts of the Laurentian channel and central
856 Scotian Shelf, and at the edge of the continental slope off the West of Vancouver Island (Fig. 13).
857 In the Arctic, areas with relatively high carbon ($> 10 \text{ kg m}^{-3}$) were predicted across many nearshore
858 areas, as well as across large parts of the Beaufort Shelf, Foxe Basin, James Bay and the Kane
859 Basin (Fig. 13). Cell specific upper and lower 95% CI bounds are shown in Figure D5. On average



860 the upper CI bounds were 54% higher than the mean prediction, and the lower CI bounds
861 less than their means.

862 Using a standardised sediment depth of 30 cm, the total standing stock of organic carbon in
863 surficial sediments across the model domain is estimated at 10.7 Gt with a 95% confidence
864 interval of 6.6 – 16.0 Gt. Between bioregions, total stock was predominantly related to the total
865 areal extent, for example Hudson Bay having the largest carbon stock and largest area (Table 2).
866 The Strait of Georgia and Southern Shelf bioregions of the Pacific had the lowest total standing
867 stocks due their small extent, however per unit area, these regions contained the highest organic
868 carbon stocks.

869



870

871 **Figure 13. Estimates of organic carbon density (kg m⁻³) across the Canadian continental margin.** The main plot
872 shows the Arctic and Atlantic regions with the Pacific region inset. The continuous variable is shown displayed in
873 discrete colour bands to improve visualisation of highly right skewed data. The 95% confidence interval bounds around
874 the predicted means are shown in Figure D5. Labels indicating the locations of different areas mentioned within the
875 text are shown in Figure A4. Country outlines from World Bank Official Boundaries, available at
876 <https://datacatalog.worldbank.org/search/dataset/0038272>.

877



878 **Table 2. Summary of estimated mean total organic carbon stocks and accumulation rates in surficial seabed**
879 **sediments of different bioregions across the Canadian continental margin.** Organic carbon standing stocks are
880 estimated for the top 30 cm of seabed sediments. For delineation of the different bioregions see Supplement.

Bioregion	Model domain extent (km ²)	OC stock (Gt)	Stock per unit area (kt km ²)	OC accumulation (Mt y ⁻¹)	Accumulation per unit area (t km ² y ⁻¹)
1. Offshore Pacific	53,598	0.14	2.67	<0.01	0.09
2. Northern Shelf BC	96,373	0.21	2.17	0.03	0.29
3. Southern Shelf BC	28,313	0.09	3.11	0.01	0.34
4. Strait of Georgia	8,664	0.04	4.56	0.05	5.31
5. Western Arctic	526,309	1.11	2.11	0.44	0.84
6. Arctic Basin	250,178	0.45	1.78	0.02	0.08
7. Arctic Archipelago	243,425	0.48	1.97	0.02	0.06
8. Eastern Arctic	757,226	1.80	2.38	0.14	0.19
9. Hudson Bay	1,234,257	3.03	2.46	1.29	1.04
10. NL Shelves	820,462	1.95	2.38	0.34	0.41
11. Gulf of St Lawrence	235,541	0.75	3.18	2.31	9.79
12. Scotian Shelf	234,888	0.61	2.59	0.21	0.90

881 Notes: OC = Organic carbon; NL = Newfoundland-Labrador.

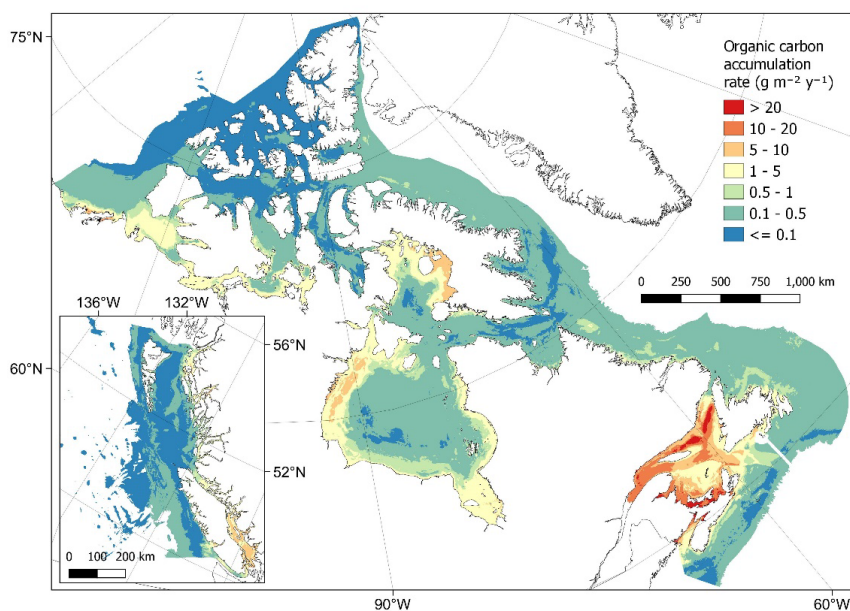
882

883 3.6 Estimated organic carbon accumulation rates

884 Organic carbon accumulation rates were estimated from combining mapped products of sediment
885 mass accumulation and organic carbon content (Fig. 2). Estimated values ranged from 3.5×10^{-6}
886 to $76.9 \text{ g m}^{-2} \text{ y}^{-1}$ with a mean of $1.1 \pm 2.8 \text{ g m}^{-2} \text{ y}^{-1}$ (\pm SD). The majority of the model domain was
887 estimated to have low accumulation rates with values $< 0.5 \text{ g m}^{-2} \text{ y}^{-1}$ (Fig. 14). Highest
888 accumulation rates were restricted to the East coast of Canada across the Gulf of St Lawrence
889 and in nearshore areas of the Bay of Fundy (Fig. 14). Other areas with relatively high
890 accumulation rates were confined to near coast areas including the Salish Sea and some fjords
891 and inlets in the Pacific west coast, as well as near coast areas in Hudson Bay, Foxe Basin and
892 the Beaufort Sea in the Arctic (Fig. 14). Cell specific upper and lower 95% CI bounds are shown
893 in Figure D6. On average the upper CI bounds were 88% higher than the mean prediction, and
894 the lower CI bounds 47% less than their means. Overall, the total accumulation of organic carbon
895 across the model domain is estimated with a mean of 4.9 Mt y^{-1} with a 95% confidence interval of
896 $2.6 - 9.3 \text{ Mt y}^{-1}$. In contrast to the organic carbon standing stock, total accumulation between
897 bioregions was not strongly related to the total areal extent. The Gulf of St Lawrence was



898 estimated to contain both the largest total annual organic carbon accumulation and the highest
899 accumulation per unit area (Table 2). The Strait of Georgia was estimated to have the second
900 highest accumulation rates per unit area, but low total carbon accumulation due to its small area
901 (Table 2). The Hudson Bay bioregion also included a large proportion of the organic carbon
902 accumulation across the model domain with the second highest total accumulation value and the
903 third highest mean per unit area (Table 2).



904

905 **Figure 14. Estimates of organic carbon accumulation rate ($\text{g m}^{-2} \text{y}^{-1}$) across the Canadian continental margin.**
906 The main plot shows the Arctic and Atlantic regions with the Pacific region inset. The continuous variable is shown
907 displayed in discrete colour bands to improve visualisation of highly right skewed data. The 95% confidence interval
908 bounds around the predicted means are shown in Figure D6. Labels indicating the locations of different areas
909 mentioned within the text are shown in Figure A4. Country outlines from World Bank Official Boundaries, available at
910 <https://datacatalog.worldbank.org/search/dataset/0038272>.

911

912 **3.7 Rock substrate distribution case studies**

913 As the predictive maps produced in this study rely on physical sediment samples alone, they are
914 unlikely to produce valid estimates for areas of bedrock - i.e. estimates of zero sediment carbon
915 density and accumulation where bedrock is located. On the Scotian shelf (bioregion 12),
916 correcting our predictive maps with a predicted bedrock distribution map (Fig. E1) reduces total



917 organic carbon stock estimates in this region by between 7.5 – 7.6% leading to a value of 0.56 Gt
918 (95% CI 0.33 – 0.87 Gt), and reducing total accumulation by 12.7 - 15.9% to a total of 0.18 Mt y⁻¹
919 (95% CI 0.08 – 0.44 Mt y⁻¹). For the Pacific British Columbian marine region (bioregions 1-4),
920 assigning zero values to areas covered by a predicted bedrock distribution map (Fig. E2) would
921 reduce our estimates by 8.5 - 9.0% to a total of 0.44 Gt (95% CI 0.26 – 0.69 Gt) for organic carbon
922 stock and reducing by 13.8 – 15.3% to a total of 0.08 Mt y⁻¹ (95% CI 0.03 – 0.23 Mt y⁻¹) for organic
923 carbon accumulation.

924

925 **4. Code and data availability**

926 All mapped products as shown in Figures 5, 8, 11, 12, 13 and 14 have been made available as
927 georeferenced TIFF files in the Borealis data repository at
928 <https://borealisdata.ca/privateurl.xhtml?token=7bb00f1e-2ce3-400c-955d-e8e0d4fe3080>
929 (Epstein et al., 2023). This includes the mean predictions as well as the cell-specific 95%
930 confidence interval bounds as shown in Appendix D. The repository also contains all data collated
931 within the systematic data review of organic carbon content and the georeferenced TIFF files from
932 the rock distribution case studies (Appendix E). Additionally, all the associated code used for data
933 manipulations, model building and predictive mapping can also be found within the above
934 repository.

935

936 **5. Discussion**

937 Using best available data, we have produced the first national assessment of organic carbon in
938 surficial seabed sediments across the Canadian continental margin, estimating the standing stock
939 in the top 30 cm to be 10.7 Gt (95% CI 6.6 – 16.0 Gt). Although comparisons to previous global
940 studies is challenging due to differences in sediment reference depths, mapping resolutions and
941 total spatial coverage, our estimate falls within a similar range to those previously published (e.g.
942 2.2 Gt in the top 5 cm (Lee et al., 2019) and 48 Gt in the top meter (Atwood et al., 2020) of the
943 Canadian EEZ). In contrast to these global studies, the national approach taken here allows for a
944 more complete data synthesis, a finer spatial resolution, larger spatial coverage of the Canadian
945 continental margin and spatially explicit estimates of uncertainty; all of which allow for higher
946 confidence in the predictive mapping products and overall estimates of standing stock. Similarly
947 to other national and regional mapping studies (Smeaton et al., 2021; Diesing et al., 2017, 2021),



948 areas of high organic carbon stocks were predominantly predicted to occur in coastal fjords, inlets,
949 estuaries, enclosed bays and sheltered basins, as well as in deeper channels and throughs (Fig.
950 13). To put our estimated organic carbon standing stock into context, 10.7 Gt equates to 51% of
951 the organic carbon estimated to be stored in all Canadian terrestrial plant live biomass and detritus
952 (both above and below ground), and 34% of soil organic carbon to 30 cm across Canada
953 (assuming equal distribution of soil carbon in the top 1 m) (Sothe et al., 2022).

954 Due to a lack of available data, we were unable to undertake a fully independent predictive
955 mapping exercise for organic carbon accumulation rates on Canadian seabed sediments.
956 However, our downscaling exercise of a recently published global product on mass accumulation
957 rates, coupled with the national predictive mapping of sediment organic carbon content, led to an
958 estimated annual accumulation at the seafloor of 4.9 Mt of organic carbon per year (95% CI 2.6
959 – 9.3 Mt y⁻¹). Given the extent of the model domain (~1.25% of the global ocean), this estimate
960 again falls close to the range of previous global predictions – i.e. 1.25% of global accumulation at
961 126–350 Mt y⁻¹ is 1.6–4.4 Mt y⁻¹ (Keil, 2017; Berner, 1982). Areas of high accumulation were
962 predominantly restricted to the Gulf of St Lawrence and Bay of Fundy, as well as other near-coast
963 areas where large river outlets co-occurred with predicted areas of high carbon density (Fig. 10,
964 13, Supplement).

965

966 *Model interpretation and uncertainties*

967 The two key components of the carbon stock estimates in this study are the predictive maps for
968 mud content and organic carbon content, which were estimated to have a map accuracy of 60%
969 and 58% respectively (R^2 0.60 and 0.58). While these values may seem relatively low when
970 compared to some other related studies (Diesing et al., 2017, 2021; Atwood et al., 2020; Mitchell
971 et al., 2019), the use of robust, spatially explicit cross-validation to calculate model evaluation
972 metrics (as we did herein) has been shown to produce significantly more conservative estimates
973 of map accuracy when compared to frequently used random cross-validation approaches (Ludwig
974 et al., 2023; Meyer et al., 2019) such as those used in both the global seabed carbon stock studies
975 discussed above (Atwood et al., 2020; Lee et al., 2019). Within this study, we also calculated cell
976 specific confidence interval bounds to give spatially explicit estimates of uncertainty. While there
977 are many ways to calculate model uncertainty, therefore making comparisons between studies
978 challenging, the uncertainty in carbon density calculated here (CI 39–54% either side of the mean)
979 is close to those found within similar regional (Diesing et al., 2021; 58%) and global studies (Lee



980 et al., 2019; 49%), both of which predict carbon stocks at significantly coarser resolutions. Our
981 95% confidence interval bounds for total standing stock (38% lower and 50% higher than the
982 mean) are also similar to the estimated bounds from the recently published predictive models of
983 Canadian terrestrial vegetation and soil carbon (a 90% confidence interval 48% either side of the
984 mean) (Sothe et al., 2022).

985 Higher map accuracy was estimated for mass accumulation rate (R^2 0.89); however, it is important
986 to recognise that this only describes the accuracy of our downscaled product to represent the
987 global spatial product from which data were sampled. This global model was itself estimated to
988 have an R^2 of 0.88 for empirical point data, however this was calculated with traditional random
989 cross-validation techniques (Restrepo et al., 2021). The estimated values of organic carbon
990 accumulation rate predicted here should be used with some caution as there is likely significant
991 uncertainty that is not truly quantified due to the small amount of *in-situ* empirical data from the
992 Canadian continental margin (Restrepo et al., 2021). The mean confidence interval for organic
993 carbon accumulation estimated in this study was also very wide at its upper bound (88% above
994 mean). This is largely due to the highly right skewed distribution of predictions, with a
995 preponderance of small accumulation rate values, meaning a small absolute increase in
996 estimated accumulation can have very large proportional effects when compared to the mean.
997 Even so, the estimates of organic carbon accumulation made here give our current best estimate
998 for the Canadian continental margin, and while the absolute values may contain high uncertainty,
999 the spatial patterns between areas across the model domain are expected to have higher
1000 confidence.

1001 Using two case studies from British Columbia and the Scotian Shelf, we estimated that the
1002 distribution of rock substrates could reduce our estimates of carbon stock by approximately 7.5 -
1003 9.0% and carbon accumulation by 12.7 – 15.3% (Fig. E1, E2). As much of the Canadian coastline
1004 is distant from significant infrastructure, extensive surveys of the seafloor are generally lacking,
1005 especially when compared to similar regional carbon mapping studies in northwest Europe (e.g.
1006 Smeaton et al., 2021). It is therefore unclear how representative these case studies are of the
1007 entire Canadian EEZ. Improved data on the presence of bedrock across lesser studied regions
1008 of the Canadian Arctic, Hudson Bay, Gulf of St Lawrence, Newfoundland and Labrador may allow
1009 for the production of a predictive map of bedrock across the Canadian EEZ which would
1010 significantly improve the carbon estimates and spatial predictive maps produced in this study.

1011 Areas of uncertainty which could not be fully quantified include the accuracy and precision of
1012 response data and predictor layers. The response data drive the model construction, and



1013 therefore sampling, processing, or recording errors can propagate into predictions. This is
1014 particularly relevant given the large temporal extent of response data which was required to gain
1015 sufficient coverage for this work (1959-2019). This large duration may also add additional variation
1016 from temporal differences between data, for example from differing anthropogenic drivers on
1017 carbon storage and/or accumulation (Keil, 2017); however, similar temporal extents have been
1018 used in related studies (Atwood et al., 2020; Lee et al., 2019; Seiter et al., 2004) and 72% of the
1019 organic carbon data within this study were sampled after 1980 and 55% after 2000. Within the
1020 response data, assumptions and/or predictions were also required regarding the distribution of
1021 mud and carbon across sediment depths. While standardising for this factor is clearly necessary,
1022 especially when using a wide variety of legacy data, it does add additional uncertainty which would
1023 not be present if widescale standardised sampling methods were employed. The results from this
1024 study do however highlight, that within the top 30 cm of sediment, the spatial location of the
1025 sample is a far stronger driver of organic carbon content than the sediment sampling depth (Table
1026 B1). Most of the predictor variables used in this study are also themselves modelled products,
1027 which contain their own inherent uncertainties and/or interpolations which cannot be fully
1028 quantified here. Additionally, many of the predictor variables have temporal components, and
1029 while the climatological mean of a 12 - 14 year timespan used in this study is expected to produce
1030 variables representative for the study region, they do not completely align with the temporal extent
1031 of the response data which could add further prediction uncertainty.

1032

1033 *Future directions and applications*

1034 Improvements could be made in future iterations of these sediment carbon maps when additional
1035 response data become available. The size of the organic carbon content dataset was relatively
1036 small (2,518 point-samples) given the size of the model domain, so new data could greatly
1037 improve accuracy and reduce uncertainty in predictions. Additionally, wide-spread *in-situ* data on
1038 sediment dry bulk density and sediment mass accumulation rates would reduce the assumptions
1039 needed in using transfer functions and downscaling models; however, large datasets would be
1040 needed to conduct robust independent modelling exercises. There are also improvements to be
1041 made with the development of higher resolution or more accurate predictor layers. This would be
1042 particularly relevant for those variables with coarse resolutions and those which were seen to
1043 have highest importance within our models or from related seabed sediment mapping studies
1044 (e.g. Gregr et al., 2021; Diesing et al., 2017, 2021; Mitchell et al., 2019) - i.e. wave velocities,
1045 suspended particulate matter, exposure, current velocities and oxygen concentrations. Further



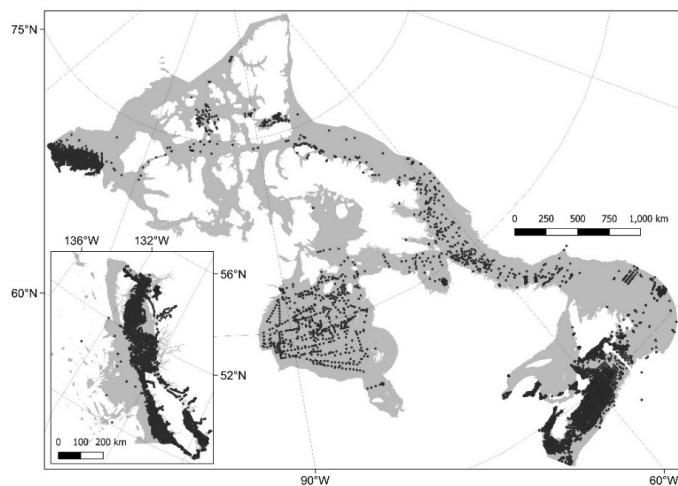
1046 validation and refinements could also be supported by numerical biogeochemical modelling
1047 products where the organic carbon densities and/or accumulations are mathematically estimated
1048 based on oceanographic, climatological and benthic conditions, including the potential to
1049 incorporate predictions under different future climate scenarios (Ani and Robson, 2021).

1050 The organic carbon predictive mapping products generated here could have many future
1051 applications. Regionalisation and prioritisation processes could identify key areas of carbon
1052 storage for further research and possible protections (Epstein and Roberts, 2022, 2023; Diesing
1053 et al., 2021). There is also potential to combine these mapped products with spatial data on
1054 human activities occurring on the seafloor to consider potential management implications, such
1055 as controlling the levels of impactful industries (e.g. mobile bottom fishing, mineral extraction,
1056 energy generation) in high organic carbon storage/accumulation areas (Clare et al., 2023; Epstein
1057 and Roberts, 2022). The mud content predictive maps may also have applications for marine
1058 planning more widely, being a strong driver of the biological habitat type and sensitivity. Overall,
1059 these data have wide-scale relevance across marine ecology, geology and environmental
1060 management disciplines, however, the use of these products should always consider the
1061 discussed uncertainties and quantified confidence interval bounds of predictions. As with all large-
1062 scale mapping exercises, continued *in-situ* empirical data collection is needed for improved
1063 accuracy of mapping seabed carbon stocks and accumulation rates across Canada.



1064 **6. Appendices**

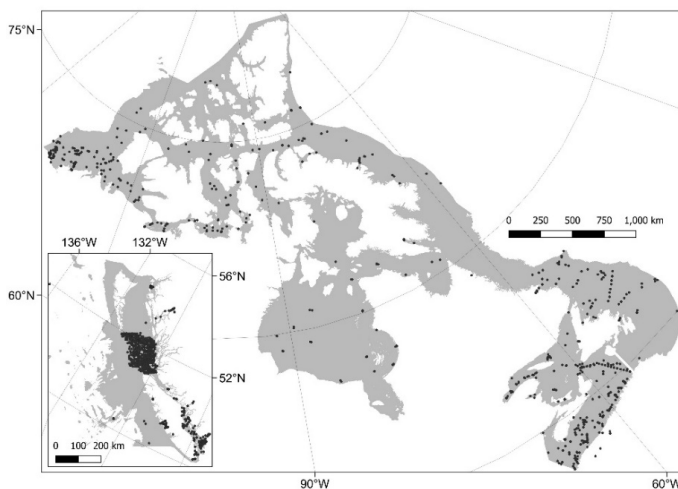
1065 **Appendix A. Distribution of response data**



1066

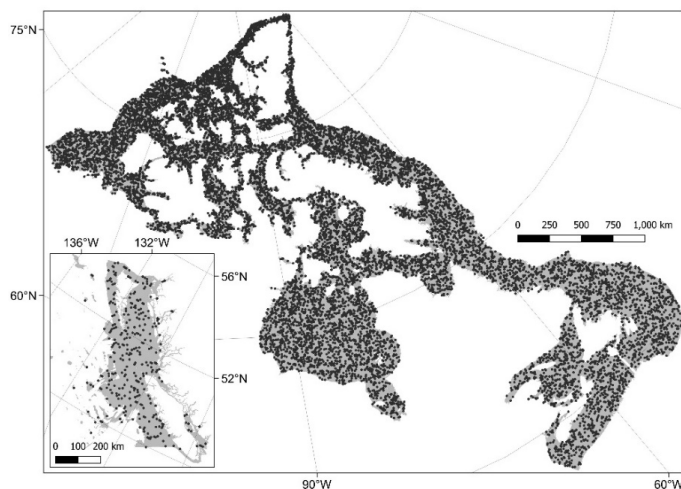
1067 **Figure A1. Map showing the distribution of mud content samples across the model domain.**

1068



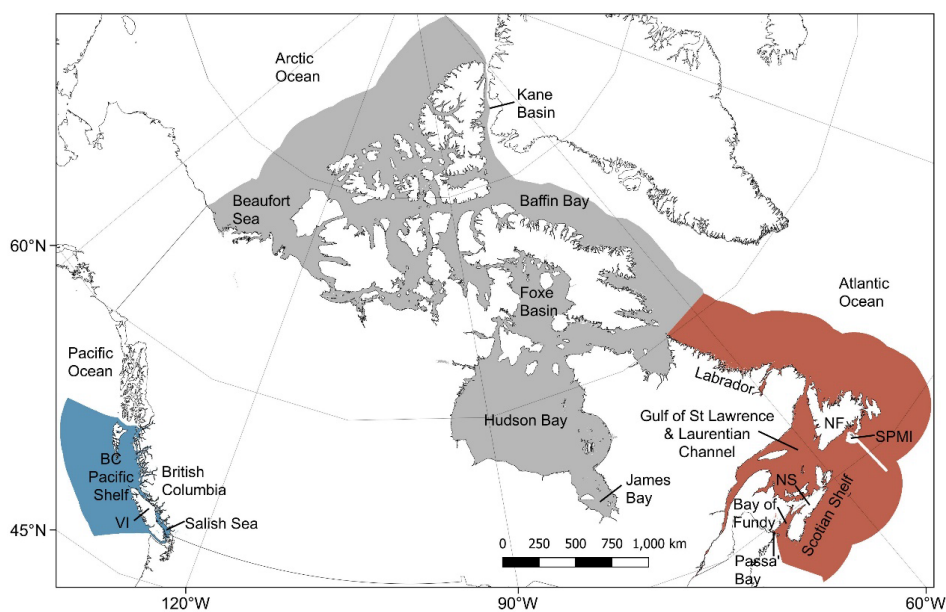
1069

1070 **Figure A2. Map showing the distribution of carbon content samples across the model domain.**



1071

1072 **Figure A3. Map showing the distribution of random-stratified sampled sediment mass accumulation rates**
1073 **across the model domain.**



1074

1075 **Figure A4. Map indicating the locations of different areas which are mentioned within the text.** The Canadian
1076 Pacific (blue), Arctic (grey) and Atlantic (red) regions are shown with labelled locations overlaid. BC = British
1077 Columbia; Passa' Bay = Passamaquoddy Bay; NS = Nova Scotia; NF = Newfoundland; SPMI = St Pierre and Miquelon.
1078 The locations are for guidance only and do not represent the entire extent or exact location of a given area. Country
1079 outlines are derived from World Bank Official Boundaries, available at
1080 <https://datacatalog.worldbank.org/search/dataset/0038272>.



1081 **Appendix B. Organic carbon sediment depth modelling results**

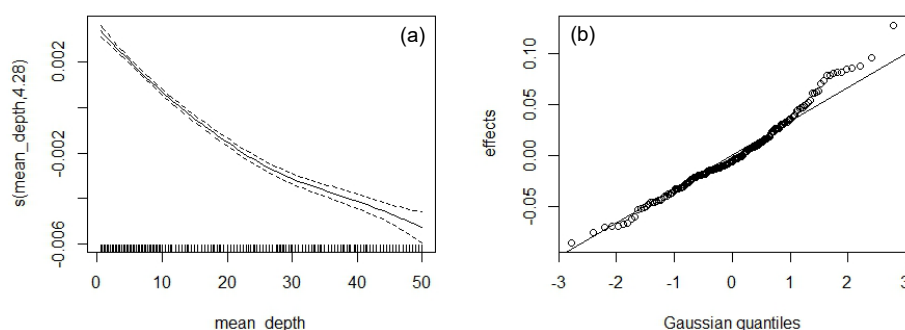
1082 There was a significant effect of sampling depth on the organic carbon content in seabed
 1083 sediments ($\chi^2 = 1400.9$, $p < 0.001$). While sample ID explained most of the variation between
 1084 sub-sample carbon contents, the sampling depth was also a significant factor (Table B1). Carbon
 1085 content decreased with increasing sampling depth (Fig. B1). The rate of carbon content decline
 1086 generally decreased with increasing depth into the sediment, however uncertainty in this trend
 1087 increased within deeper sediment layers (Fig. B1).

1088

1089 **Table B1. Results from the generalised additive mixed model between the carbon content of marine sediments**
 1090 **and sampling depth.** A basic generalised additive mixed model with a scaled-t distribution was constructed for carbon
 1091 content in sediment sub-samples with sample ID as the random factor and sampling depth as the fixed factor.

Spline	Type	edf	Res. df	χ^2	Deviance explained	p
Sampling depth (cm)	Cubic	4.28	5.36	2299	1.1%	< 0.001
ID	Random	181.94	182.00	715046	86.9%	< 0.001

1092 Notes: edf = Effective degrees of freedom. Res. df = Residual degrees of freedom



1093

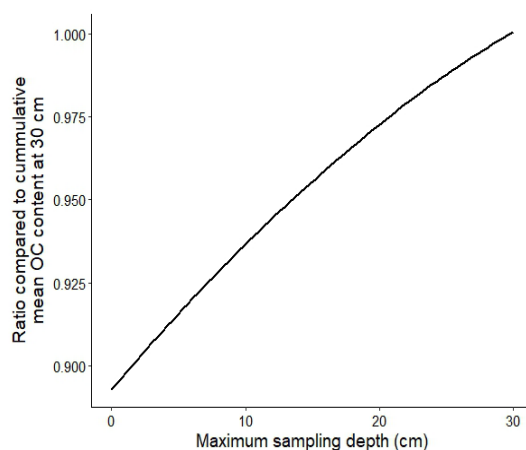
1094 **Figure B1. Regression splines indicating the effect of sediment sampling depth (a) and sample ID (b) on the**
 1095 **organic carbon content in seabed sediment sub-samples.**

1096

1097 The predicted mean effect of sediment depth on carbon content was extracted from the model
 1098 and converted into a transfer function which states the expected ratio between the cumulative
 1099 carbon content at 30 cm compared to any given sampling depth (Figure B2). The ratio ranged
 1100 from 89.3% when only measuring the sediment surface, to 93.7% if measuring the carbon content
 1101 across the top 10 cm, and by 25 cm was approaching equilibrium at 98.8%.



1102

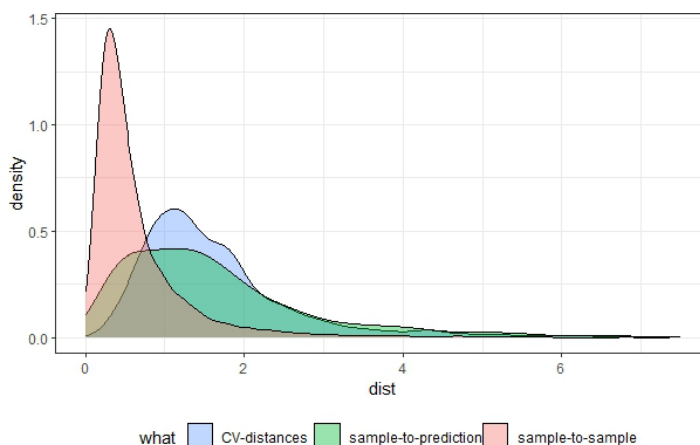


1103

1104 **Figure B2. Transfer function for cumulative mean organic carbon (OC) content at 30 cm sediment depth.** Using
1105 a generalised additive mixed model an estimated transfer function was constructed to standardise the cumulative mean
1106 carbon content at any given depth to an expected value at 30 cm.

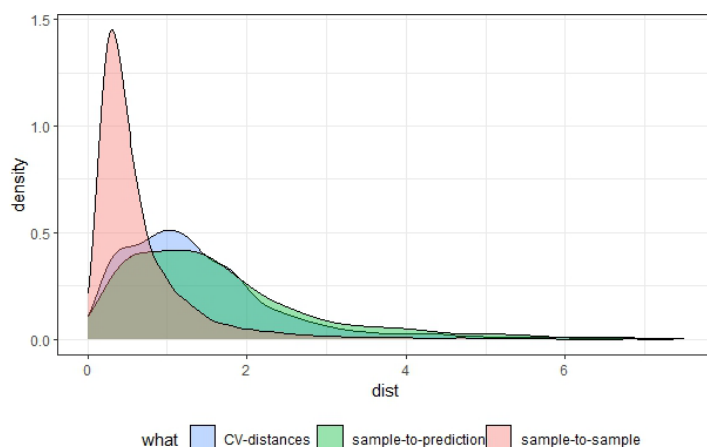
1107

1108 Appendix C. Results from random forest cross-validation structure selection



1109

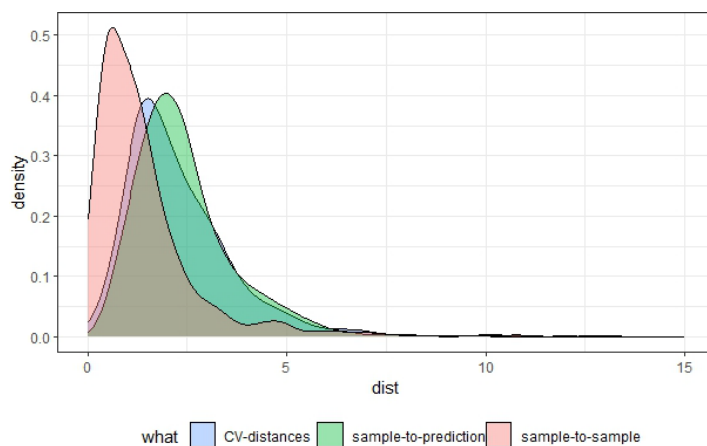
1110 **Figure C1. Multivariate nearest-neighbour distance density plot for mud content data with the optimal number**
1111 **of spatial k-means clusters across cross validation (CV) folds.** Frequency of nearest neighbour distances (x-axis)
1112 is shown for sample-to-sample distance (red), sample-to-prediction distance (green) and CV fold analysis-to-
1113 assessment distance (blue). An optimal number of 35 clusters was selected to due close overlap between the CV-
1114 distance and sample-to-prediction curve.



1115

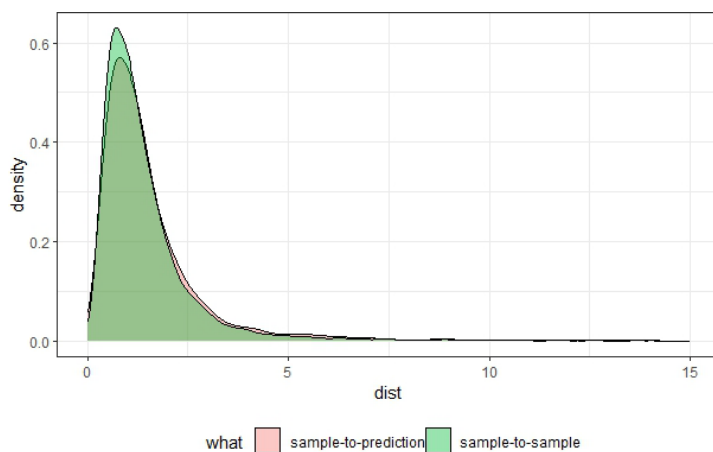
1116 **Figure C2. Multivariate nearest-neighbour distance density plot for mud content data with a partially repeated**
1117 **spatial-random mixture method for cross validation (CV) folds.** Frequency of nearest neighbour distances (x-axis)
1118 is shown for sample-to-sample distance (red), sample-to-prediction distance (green) and CV fold analysis-to-
1119 assessment distance (blue). Due to the optimal spatial k-means clustering showing poor overlap at lower multivariate
1120 distances (Fig. C1), a 1% random sample without replacement was added to each fold.

1121



1122

1123 **Figure C3. Multivariate nearest neighbour distance density plot for organic carbon content data with the**
1124 **optimal block size across cross validation (CV) folds.** Frequency of nearest neighbour distances (x-axis) is shown
1125 for sample-to-sample distance (red), sample-to-prediction distance (green) and CV fold analysis-to-assessment
1126 distance (blue). An optimal block size of 100 km was selected to due close overlap between the CV-distance and
1127 sample-to-prediction curve.



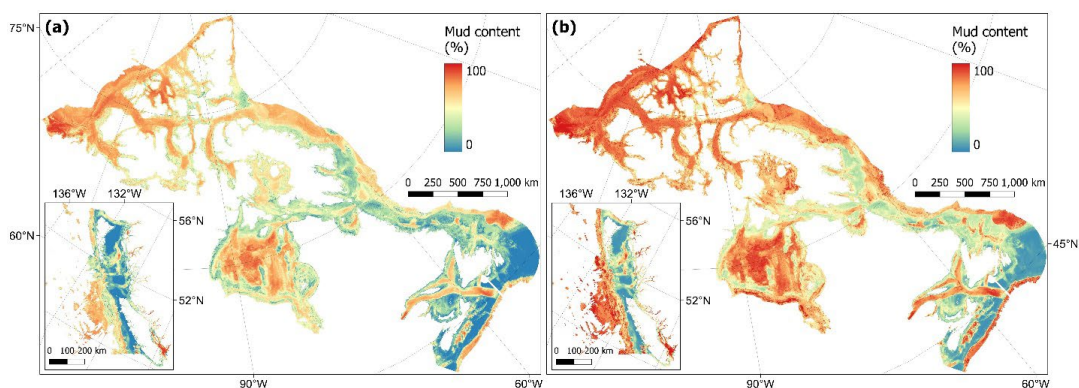
1128

1129 **Figure C4. Multivariate nearest neighbour density plot for sediment mass accumulation rate data.** Frequency of
1130 nearest neighbour distances (x-axis) is shown for sample-to-sample distance (red) and sample-to-prediction
1131 (green). The close overlap indicates that random cross-validation will produce valid results.

1132



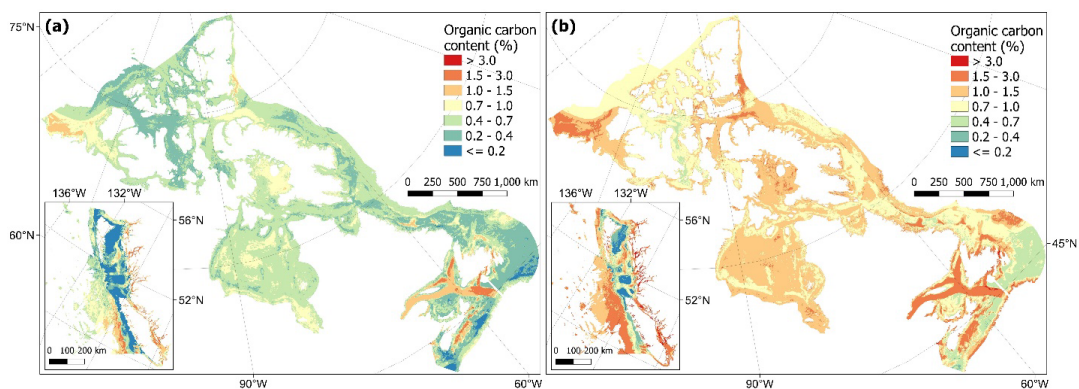
1133 **Appendix D. Cell-specific confidence interval bounds for predictive sediment maps**



1134

1135 **Figure D1. Estimated lower (a) and upper (b) bounds of the 95% confidence interval for predictions of mud**
1136 **content (%) in subtidal marine sediments across the Canadian continental margin.** Within each panel the main
1137 plot shows the Arctic and Atlantic regions with the Pacific region inset.

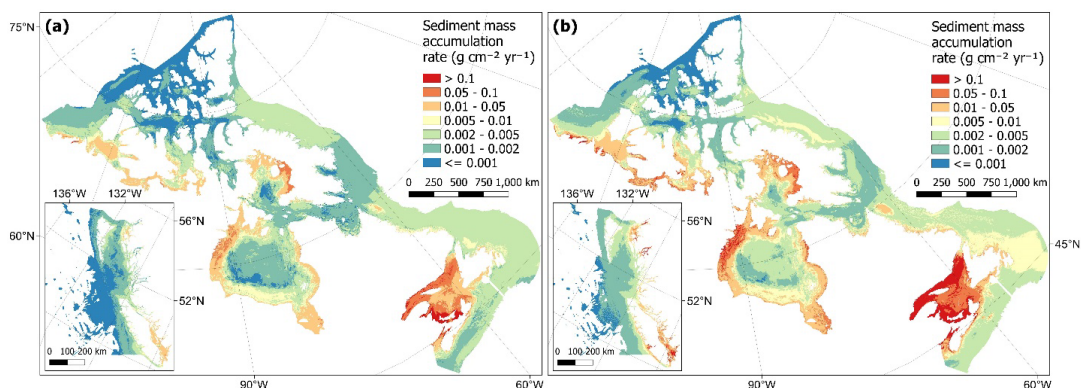
1138



1139

1140 **Figure D2. Estimated lower (a) and upper (b) bounds of the 95% confidence interval for predictions of carbon**
1141 **content (%) in subtidal marine sediments across the Canadian continental margin.** The continuous variable is
1142 shown in discrete colour bands to improve visualisation of highly right skewed data. Within each panel the
1143 main plot shows the Arctic and Atlantic regions with the Pacific region inset.

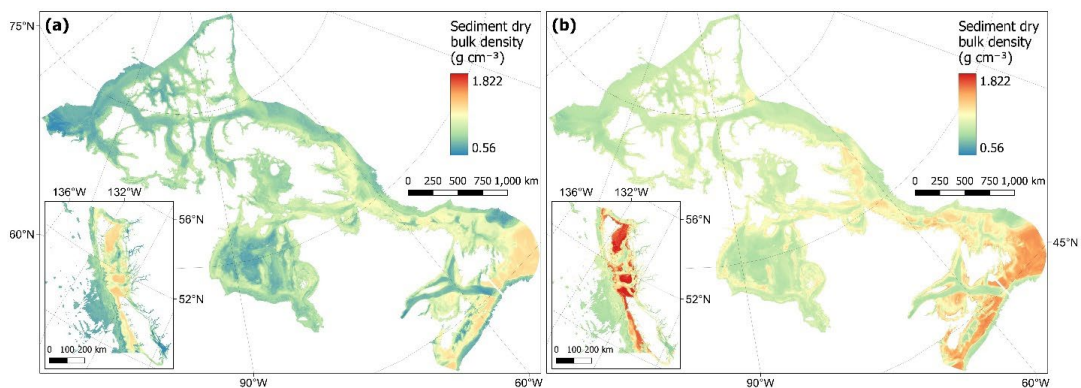
1144



1145

1146 **Figure D3. Estimated lower (a) and upper (b) bounds of the 95% confidence interval for predictions of mass**
1147 **accumulation rate ($\text{g cm}^{-2} \text{yr}^{-1}$) on subtidal marine sediments across the Canadian continental margin. The**
1148 **continuous variable is shown in discrete colour bands to improve visualisation of highly right skewed data. Within each**
1149 **panel the main plot shows the Arctic and Atlantic regions with the Pacific region inset.**

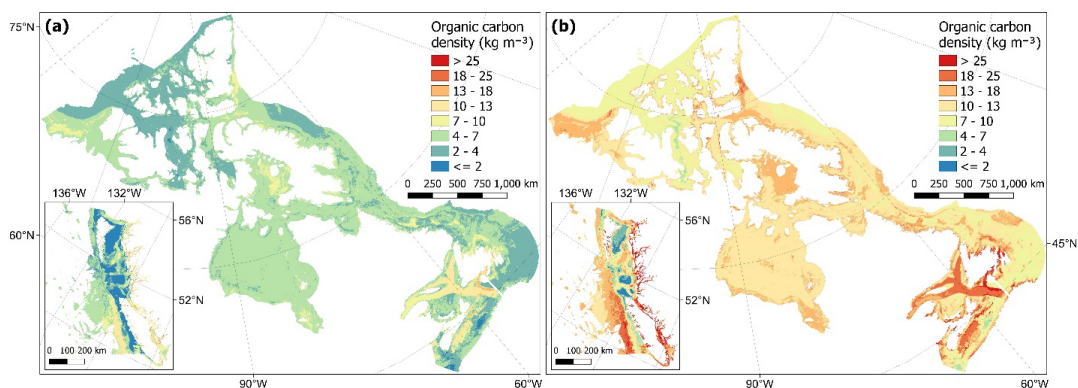
1150



1151

1152 **Figure D4. Estimated lower (a) and upper (b) bounds of the 95% confidence interval for predictions of dry bulk**
1153 **density (g cm^{-3}) of subtidal marine sediments across the Canadian continental margin. Within each panel the**
1154 **main plot shows the Arctic and Atlantic regions with the Pacific region inset.**

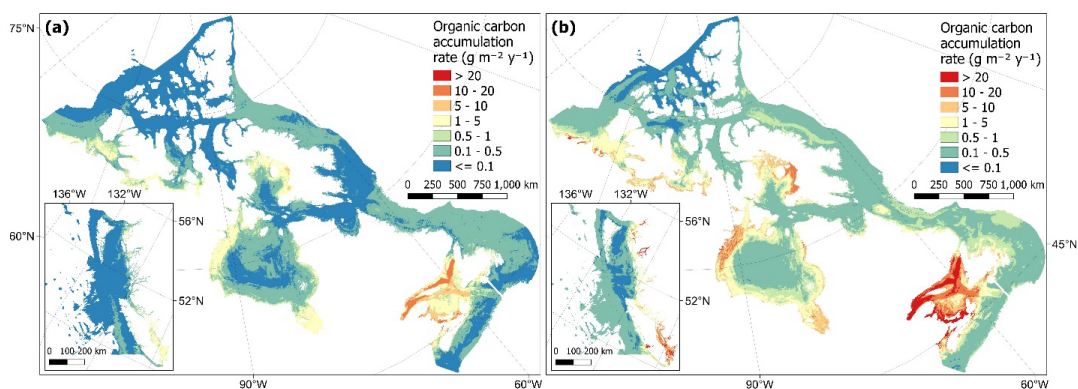
1155



1156

1157 **Figure D5. Estimated lower (a) and upper (b) bounds of the 95% confidence interval for predictions of organic**
1158 **carbon density (kg m^{-3}) in subtidal marine sediments across the Canadian continental margin.** The continuous
1159 variable is shown in discrete colour bands to improve visualisation of highly right skewed data. Within each panel the
1160 main plot shows the Arctic and Atlantic regions with the Pacific region inset.

1161



1162

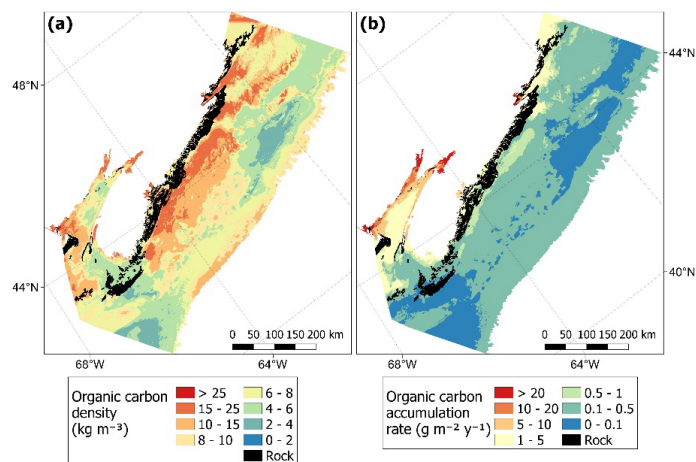
1163 **Figure D6. Estimated lower (a) and upper (b) bounds of the 95% confidence interval for predictions of organic**
1164 **carbon accumulation rates ($\text{g m}^{-2} \text{y}^{-1}$) on subtidal marine sediments across the Canadian continental margin.**
1165 The continuous variable is shown in discrete colour bands to improve visualisation of highly right skewed data. Within
1166 each panel the main plot shows the Arctic and Atlantic regions with the Pacific region inset.

1167

1168



1169 Appendix E. Bedrock distribution case studies

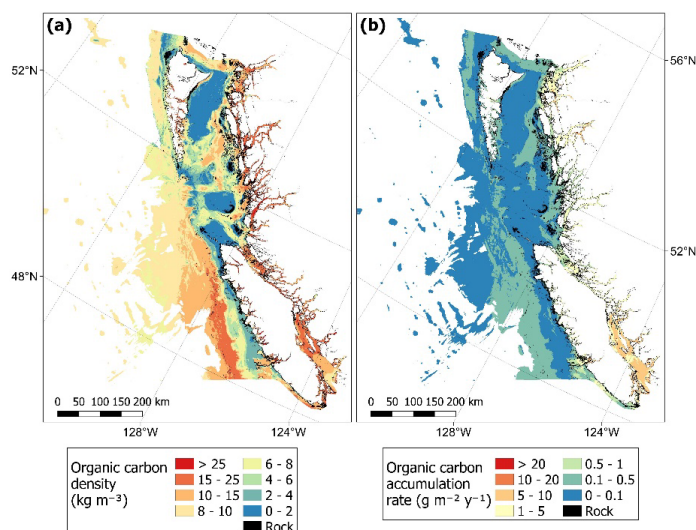


1170

1171 **Figure E1. Predicted mean values of organic carbon density and accumulation rates within the Scotian Shelf**
1172 **overlayed by the estimated distribution of rock substrates.** Data on the estimated distribution of rock on the
1173 seafloor across the Scotian Shelf Bioregion is taken from Philibert et al. (2022).

1174

1175



1176

1177 **Figure E2. Predicted mean values of organic carbon density and accumulation rates within the British**
1178 **Columbia EEZ overlayed by the estimated distribution of rock substrates.** Data on the estimated distribution of
1179 rock on the seafloor across the British Columbian continental margin is taken from Gregr et al. (2021).



1180 **7. Author contributions**

1181 JKB and SDF secured funding and led the management of this project. GE, SDF and JKB
1182 conceptualised this study. GE, DH, AP, CP & PGM collated the data. GE developed the model
1183 code and performed the investigations with input from SDF and JKB throughout. GE prepared the
1184 manuscript with contributions from all co-authors.

1185

1186 **8. Competing interests**

1187 The authors declare that they have no conflict of interest.

1188

1189 **9. Acknowledgements**

1190 We would like to thank Randy Enkin, Sarah Paradis and Genevieve Philibert for providing data
1191 towards this work. We also greatly appreciate advice given across various stages of the
1192 processes from Cooper Stacey, Markus Diesing, Ashley Park, Nadja Steiner, Diane Lavoie,
1193 Amber Holdsworth, Sophia Johannessen, Michael Li, Kate Jarret, Javier Murillo-Perez, Ellen
1194 Kenchington, Emily Rubidge and others within the Department for Fisheries and Oceans, and
1195 Natural Resources Canada. We would also like to thank Jennifer McHenry, Matt Csordas and
1196 Brian Timmer for their ideas in trouble-shooting discussions. This research was enabled in part
1197 by support provided by BC & Prairies Digital Research Infrastructure and the Digital Research
1198 Alliance of Canada (alliancecan.ca).

1199

1200 **10. Financial support**

1201 This work was funded by an Natural Sciences and Engineering Research Council (NSERC)
1202 Alliance partnership grant #ALLRP571068 – 21 to JKB, and is publication #001 of Blue Carbon
1203 Canada. GE is also supported by a Mitacs-Accelerate Fellowship, jointly funded by Oceans North.
1204 PGM also gratefully acknowledge the financial and logistic support of grants from NSERC
1205 including a Discovery Grant (rgpin 227438-09) and Climate Change and Atmospheric Research
1206 Grants (VITALS - RGPC433898 and the Canadian Arctic Geotraces program - RGPC
1207 433848), as well as support from the Marine Environmental Observation, Prediction and
1208 Response Network (MEOPAR) Prediction Core.



1209 11. References

- 1210 Amoroso, R. O., Pitcher, C. R., Rijnsdorp, A. D., McConnaughey, R. A., Parma, A. M., Suuronen, P.,
1211 Eigaard, O. R., Bastardie, F., Hintzen, N. T., Althaus, F., Baird, S. J., Black, J., Buhl-Mortensen, L.,
1212 Campbell, A. B., Catarino, R., Collie, J., Cowan, J. H., Jr., Durholtz, D., Engstrom, N., Fairweather, T. P.,
1213 Fock, H. O., Ford, R., Galvez, P. A., Gerritsen, H., Gongora, M. E., Gonzalez, J. A., Hiddink, J. G., Hughes, K.
1214 M., Intelmann, S. S., Jenkins, C., Jonsson, P., Kainge, P., Kangas, M., Kathena, J. N., Kavadas, S., Leslie, R.
1215 W., Lewis, S. G., Lundy, M., Makin, D., Martin, J., Mazor, T., Gonzalez-Mirelis, G., Newman, S. J.,
1216 Papadopoulou, N., Posen, P. E., Rochester, W., Russo, T., Sala, A., Semmens, J. M., Silva, C., Tsolos, A.,
1217 Vanellander, B., Wakefield, C. B., Wood, B. A., Hilborn, R., Kaiser, M. J., and Jennings, S.: Bottom trawl
1218 fishing footprints on the world's continental shelves, *Proceedings of the National Academy of Sciences*
1219 of the USA, 115, E10275–E10282, <https://doi.org/10.1073/pnas.1802379115>, 2018.
- 1220 Ani, C. J. and Robson, B.: Responses of marine ecosystems to climate change impacts and their
1221 treatment in biogeochemical ecosystem models, *Marine Pollution Bulletin*, 166, 112223,
1222 <https://doi.org/10.1016/j.marpolbul.2021.112223>, 2021.
- 1223 Arndt, S., Jørgensen, B. B., LaRowe, D. E., Middelburg, J. J., Pancost, R. D., and Regnier, P.: Quantifying
1224 the degradation of organic matter in marine sediments: A review and synthesis, *Earth-Science Reviews*,
1225 123, 53–86, <https://doi.org/10.1016/j.earscirev.2013.02.008>, 2013.
- 1226 Assis, J., Tyberghein, L., Bosch, S., Verbruggen, H., Serrão, E. A., and De Clerck, O.: Bio-ORACLE v2.0:
1227 Extending marine data layers for bioclimatic modelling, *Global Ecology and Biogeography*, 27, 277–284,
1228 <https://doi.org/10.1111/geb.12693>, 2018.
- 1229 Atwood, T. B., Witt, A., Mayorga, J., Hammill, E., and Sala, E.: Global Patterns in Marine Sediment Carbon
1230 Stocks, *Frontiers in Marine Science*, 7, 165, <https://doi.org/10.3389/fmars.2020.00165>, 2020.
- 1231 Avelar, S., van der Voort, T. S., and Eglinton, T. I.: Relevance of carbon stocks of marine sediments for
1232 national greenhouse gas inventories of maritime nations, *Carbon Balance and Management*, 12, 10,
1233 <https://doi.org/10.1186/s13021-017-0077-x>, 2017.
- 1234 Bauer, J. E., Cai, W.-J., Raymond, P. A., Bianchi, T. S., Hopkinson, C. S., and Regnier, P. A. G.: The changing
1235 carbon cycle of the coastal ocean, *Nature*, 504, 61–70, <https://doi.org/10.1038/nature12857>, 2013.
- 1236 Berner, R. A.: Burial of organic carbon and pyrite sulfur in the modern ocean; its geochemical and
1237 environmental significance, *American Journal of Science*, 282, 451–473,
1238 <https://doi.org/10.2475/ajs.282.4.451>, 1982.
- 1239 Burdige, D. J.: Preservation of Organic Matter in Marine Sediments: Controls, Mechanisms, and an
1240 Imbalance in Sediment Organic Carbon Budgets?, *Chemical Reviews*, 107, 467–485,
1241 <https://doi.org/10.1021/cr050347q>, 2007.
- 1242 Cavan, E. L. and Hill, S. L.: Commercial fishery disturbance of the global ocean biological carbon sink,
1243 *Global Change Biology*, 28, 1212–1221, <https://doi.org/10.1111/gcb.16019>, 2022.
- 1244 Clare, M. A., Lichtschlag, A., Paradis, S., and Barlow, N. L. M.: Assessing the impact of the global subsea
1245 telecommunications network on sedimentary organic carbon stocks, *Nature Communications*, 14, 2080,
1246 <https://doi.org/10.1038/s41467-023-37854-6>, 2023.



- 1247 Copernicus: Arctic Ocean Wave Hindcast - ARCTIC_MULTIYEAR_WAV_002_013 - Norwegian
1248 Meteorological Institute, Copernicus Marine Data Store, <https://doi.org/10.48670/moi-00008>, 2022a.
- 1249 Copernicus: Global Ocean Colour (GlobColour) - ACRI - OCEANCOLOUR_GLO_BGC_L3_MY_009_103 -
1250 Bio-Geo-Chemical, L3 (daily) from Satellite Observations (1997-ongoing), Copernicus Marine Data Store,
1251 <https://doi.org/10.48670/moi-00280>, 2022b.
- 1252 Copernicus: Global Ocean Waves Reanalysis - WAVERYS - GLOBAL_MULTIYEAR_WAV_001_032 -
1253 Mercator Océan International, Copernicus Marine Data Store, <https://doi.org/10.48670/moi-00022>,
1254 2022c.
- 1255 DFO: Federal Marine Bioregions, Fisheries and Oceans Canada, 2022.
- 1256 Diesing, M., Kroger, S., Parker, R., Jenkins, C., Mason, C., and Weston, K.: Predicting the standing stock of
1257 organic carbon in surface sediments of the North-West European continental shelf, *Biogeochemistry*,
1258 135, 183–200, <https://doi.org/10.1007/s10533-017-0310-4>, 2017.
- 1259 Diesing, M., Thorsnes, T., and Bjarnadóttir, L. R.: Organic carbon densities and accumulation rates in
1260 surface sediments of the North Sea and Skagerrak, *Biogeosciences*, 18, 2139–2160,
1261 <https://doi.org/10.5194/bg-18-2139-2021>, 2021.
- 1262 Duarte, C. M., Middelburg, J. J., and Caraco, N.: Major role of marine vegetation on the oceanic carbon
1263 cycle, *Biogeosciences*, 2, 1–8, 2005.
- 1264 Enkin, J. R.: Sediment Grain Size Distribution Measurements, from Canadian Pacific Seafloor Samples,
1265 Collected from 1951 to 2017, Geological survey of Canada Open File, in press, 2023.
- 1266 Epstein, G. and Roberts, C. M.: Identifying priority areas to manage mobile bottom fishing on seabed
1267 carbon in the UK, *PLOS Climate*, 1, e0000059, <https://doi.org/10.1371/journal.pclm.0000059>, 2022.
- 1268 Epstein, G. and Roberts, C. M.: Does biodiversity-focused protection of the seabed deliver carbon
1269 benefits? A U.K. case study, *Conservation Letters*, 16, e12929, <https://doi.org/10.1111/conl.12929>,
1270 2023.
- 1271 Epstein, G., Middelburg, J. J., Hawkins, J. P., Norris, C. R., and Roberts, C. M.: The impact of mobile
1272 demersal fishing on carbon storage in seabed sediments, *Global Change Biology*, 28, 2875–2894,
1273 <https://doi.org/10.1111/gcb.16105>, 2022.
- 1274 Epstein, G., Fuller, S. D., Hingmire, D., Myers, P., Peña, A., Pennelly, C., and Baum, J. K.: Predictive maps
1275 and related data on organic carbon stocks and accumulation rates in surficial sediments of the Canadian
1276 continental margin. [https://borealisdata.ca/privateurl.xhtml?token=7bb00f1e-2ce3-400c-955d-](https://borealisdata.ca/privateurl.xhtml?token=7bb00f1e-2ce3-400c-955d-e8e0d4fe3080)
1277 [e8e0d4fe3080](https://borealisdata.ca/privateurl.xhtml?token=7bb00f1e-2ce3-400c-955d-e8e0d4fe3080), Borealis, DRAFT VERSION, UNF:6:vYJjKEPuOf4yOyxq1b4dFg== [fileUNF], 2023.
- 1278 Evans, J. S. and Murphy, M. A.: spatialEco, R package version 1.3-6, 2021.
- 1279 Flanders Marine Institute: Boundaries of Canda EEZ - mrgid 8493, Maritime Boundaries Geodatabase:
1280 Maritime Boundaries and Exclusive Economic Zones (200NM), version 11.,
1281 <https://doi.org/10.14284/386>, 2019.



- 1282 GEBCO: GEBCO Compilation Group - GEBCO_2022 Grid, The General Bathymetric Chart of the Oceans,
1283 <https://doi.org/10.5285/e0f0bb80-ab44-2739-e053-6c86abc0289c>, 2022.
- 1284 Gräler, B., Pebesma, E., and Heuvelink, G.: Spatio-Temporal Interpolation using gstat, *The R Journal*, 8,
1285 204–218, 2016.
- 1286 Graw, J. H., Wood, W. T., and Phrampus, B. J.: Predicting Global Marine Sediment Density Using the
1287 Random Forest Regressor Machine Learning Algorithm, *Journal of Geophysical Research: Solid Earth*,
1288 126, e2020JB020135, <https://doi.org/10.1029/2020JB020135>, 2021.
- 1289 Gregr, E. J., Haggarty, D. R., Davies, S. C., Fields, C., and Lessard, J.: Comprehensive marine substrate
1290 classification applied to Canada’s Pacific shelf, *PLOS ONE*, 16, 1–28,
1291 <https://doi.org/10.1371/journal.pone.0259156>, 2021.
- 1292 Gudmundsson, L., Bremnes, J. B., Haugen, J. E., and Engen-Skaugen, T.: Technical Note: Downscaling
1293 RCM precipitation to the station scale using statistical transformations – a comparison of
1294 methods, *Hydrology and Earth System Sciences*, 16, 3383–3390, [https://doi.org/10.5194/hess-16-3383-](https://doi.org/10.5194/hess-16-3383-2012)
1295 2012, 2012.
- 1296 Halpern, B. S., Frazier, M., Afflerbach, J., Lowndes, J. S., Micheli, F., O’Hara, C., Scarborough, C., and
1297 Selkoe, K. A.: Recent pace of change in human impact on the world’s ocean, *Scientific Reports*, 9, 11609,
1298 <https://doi.org/10.1038/s41598-019-47201-9>, 2019.
- 1299 Hiddink, J. G., van de Velde, S. J., McConnaughey, R. A., De Berger, E., Tiano, J., Kaiser, M. J., Sweetman,
1300 A. K., and Sciberras, M.: Quantifying the carbon benefits of ending bottom trawling, *Nature*, 617, E1–E2,
1301 <https://doi.org/10.1038/s41586-023-06014-7>, 2023.
- 1302 Hijmans, R. J.: terra: Spatial Data Analysis, R package version 1.5-21, [https://CRAN.R-](https://CRAN.R-project.org/package=terra)
1303 [project.org/package=terra](https://CRAN.R-project.org/package=terra), 2022.
- 1304 Hilborn, R. and Kaiser, M. J.: A path forward for analysing the impacts of marine protected areas, *Nature*,
1305 607, E1–E2, <https://doi.org/10.1038/s41586-022-04775-1>, 2022.
- 1306 Hoegh-Guldberg, O., Lovelock, C., Caldeira, K., Howard, J., Chopin, T., and Gaines, S.: The ocean as a
1307 solution to climate change: five opportunities for action, World Resources Institute, Washington, DC,
1308 2019.
- 1309 Hu, X., Myers, P. G., and Lu, Y.: Pacific Water Pathway in the Arctic Ocean and Beaufort Gyre in Two
1310 Simulations With Different Horizontal Resolutions, *Journal of Geophysical Research: Oceans*, 124, 6414–
1311 6432, <https://doi.org/10.1029/2019JC015111>, 2019.
- 1312 Hülse, D., Arndt, S., Wilson, J. D., Munhoven, G., and Ridgwell, A.: Understanding the causes and
1313 consequences of past marine carbon cycling variability through models, *Earth-Science Reviews*, 171,
1314 349–382, <https://doi.org/10.1016/j.earscirev.2017.06.004>, 2017.
- 1315 Ilich, A. R., Misiuk, B., Lecours, V., and Lecours, S. A.: MultiscaledDTM,
1316 <https://doi.org/10.5281/zenodo.5548338>, 2021.



- 1317 IPCC: 2019 Refinement to the 2006 IPCC Guidelines for National Greenhouse Gas Inventories, The
1318 International Plant Protection Convention, 2019.
- 1319 Jakobsson, M., Mayer, L. A., Bringensparr, C., Castro, C. F., Mohammad, R., Johnson, P., Ketter, T.,
1320 Accettella, D., Amblas, D., An, L., Arndt, J. E., Canals, M., Casamor, J. L., Chauché, N., Coakley, B.,
1321 Danielson, S., Demarte, M., Dickson, M.-L., Dorschel, B., Dowdeswell, J. A., Dreutter, S., Fremand, A. C.,
1322 Gallant, D., Hall, J. K., Hehemann, L., Hodnesdal, H., Hong, J., Ivaldi, R., Kane, E., Klaucke, I., Krawczyk, D.
1323 W., Kristoffersen, Y., Kuipers, B. R., Millan, R., Masetti, G., Morlighem, M., Noormets, R., Prescott, M. M.,
1324 Rebesco, M., Rignot, E., Semiletov, I., Tate, A. J., Travaglini, P., Velicogna, I., Weatherall, P., Weinrebe,
1325 W., Willis, J. K., Wood, M., Zarayskaya, Y., Zhang, T., Zimmermann, M., and Zinglensen, K. B.: The
1326 International Bathymetric Chart of the Arctic Ocean Version 4.0, *Scientific Data*, 7, 176,
1327 <https://doi.org/10.1038/s41597-020-0520-9>, 2020.
- 1328 Jenkins, C. J.: Summary of the onCALCULATION methods used in dbSEABED, in: Buczkowski, B.J., Reid,
1329 J.A., Jenkins, C.J., Reid, J.M., Williams, S.J., and Flocks, J.G. usSEABED: Gulf of Mexico and Caribbean
1330 (Puerto Rico and U.S. Virgin Islands) Offshore Surficial Sediment Data Release: U.S. United States
1331 Geological Survey, 2005.
- 1332 Keil, R.: Anthropogenic Forcing of Carbonate and Organic Carbon Preservation in Marine Sediments,
1333 *Annual Review of Marine Science*, 9, 151–172, <https://doi.org/10.1146/annurev-marine-010816-060724>, 2017.
- 1335 Kuhn, M.: caret: Classification and Regression Training, R package version 6.0-93, 2022.
- 1336 Kuhn, M. and Wickham, H.: Tidymodels: a collection of packages for modeling and machine learning
1337 using tidyverse principles, 2020.
- 1338 Kuzyk, Z. Z. A., Gobeil, C., Goñi, M. A., and Macdonald, R. W.: Early diagenesis and trace element
1339 accumulation in North American Arctic margin sediments, *Geochimica et Cosmochimica Acta*, 203, 175–
1340 200, <https://doi.org/10.1016/j.gca.2016.12.015>, 2017.
- 1341 LaRowe, D. E., Arndt, S., Bradley, J. A., Burwicz, E., Dale, A. W., and Amend, J. P.: Organic carbon and
1342 microbial activity in marine sediments on a global scale throughout the Quaternary, *Geochimica et*
1343 *Cosmochimica Acta*, 286, 227–247, <https://doi.org/10.1016/j.gca.2020.07.017>, 2020a.
- 1344 LaRowe, D. E., Arndt, S., Bradley, J. A., Estes, E. R., Hoarfrost, A., Lang, S. Q., Lloyd, K. G., Mahmoudi, N.,
1345 Orsi, W. D., Shah Walter, S. R., Steen, A. D., and Zhao, R.: The fate of organic carbon in marine sediments
1346 - New insights from recent data and analysis, *Earth-Science Reviews*, 204,
1347 <https://doi.org/10.1016/j.earscirev.2020.103146>, 2020b.
- 1348 Lee, T. R., Wood, W. T., and Phrampus, B. J.: A Machine Learning (kNN) Approach to Predicting Global
1349 Seafloor Total Organic Carbon, *Global Biogeochemical Cycles*, 33, 37–46,
1350 <https://doi.org/10.1029/2018gb005992>, 2019.
- 1351 Legge, O., Johnson, M., Hicks, N., Jickells, T., Diesing, M., Aldridge, J., Andrews, J., Artioli, Y., Bakker, D. C.
1352 E., Burrows, M. T., Carr, N., Cripps, G., Felgate, S. L., Fernand, L., Greenwood, N., Hartman, S., Kröger, S.,
1353 Lessin, G., Mahaffey, C., Mayor, D. J., Parker, R., Queirós, A. M., Shutler, J. D., Silva, T., Stahl, H., Tinker,
1354 J., Underwood, G. J. C., Van Der Molen, J., Wakelin, S., Weston, K., and Williamson, P.: Carbon on the



- 1355 Northwest European Shelf: Contemporary Budget and Future Influences, *Frontiers in Marine Science*, 7,
1356 Article 143, <https://doi.org/10.3389/fmars.2020.00143>, 2020.
- 1357 Ludwig, M., Moreno-Martinez, A., Hölzel, N., Pebesma, E., and Meyer, H.: Assessing and improving the
1358 transferability of current global spatial prediction models, *Global Ecology and Biogeography*, 32, 356–
1359 368, <https://doi.org/10.1111/geb.13635>, 2023.
- 1360 Luisetti, T., Turner, R. K., Andrews, J. E., Jickells, T. D., Kröger, S., Diesing, M., Paltriguera, L., Johnson, M.
1361 T., Parker, E. R., Bakker, D. C. E., and Weston, K.: Quantifying and valuing carbon flows and stores in
1362 coastal and shelf ecosystems in the UK, *Ecosystem Services*, 35, 67–76,
1363 <https://doi.org/10.1016/j.ecoser.2018.10.013>, 2019.
- 1364 Luisetti, T., Ferrini, S., Grilli, G., Jickells, T. D., Kennedy, H., Kröger, S., Lorenzoni, I., Milligan, B., van der
1365 Molen, J., Parker, R., Pryce, T., Turner, R. K., and Tyllianakis, E.: Climate action requires new accounting
1366 guidance and governance frameworks to manage carbon in shelf seas, *Nature Communications*, 11,
1367 4599, <https://doi.org/10.1038/s41467-020-18242-w>, 2020.
- 1368 Macreadie, P. I., Costa, M. D. P., Atwood, T. B., Friess, D. A., Kelleway, J. J., Kennedy, H., Lovelock, C. E.,
1369 Serrano, O., and Duarte, C. M.: Blue carbon as a natural climate solution, *Nature Reviews Earth &
1370 Environment*, 2, 826–839, <https://doi.org/10.1038/s43017-021-00224-1>, 2021.
- 1371 Madec, G., Delecluse, P., Imbard, M., and Lévy, C.: OPA 8.1 Ocean General Circulation Model, Technical
1372 Report of LODYC/IPSL, Note 11, 1998.
- 1373 Martin, K. M., Wood, W. T., and Becker, J. J.: A global prediction of seafloor sediment porosity using
1374 machine learning, *Geophysical Research Letters*, 42, 10,640–10,646,
1375 <https://doi.org/10.1002/2015GL065279>, 2015.
- 1376 Masson, D. and Fine, I.: Modeling seasonal to interannual ocean variability of coastal British Columbia,
1377 *Journal of Geophysical Research: Oceans*, 117, <https://doi.org/10.1029/2012JC008151>, 2012.
- 1378 Meyer, H. and Pebesma, E.: Machine learning-based global maps of ecological variables and the
1379 challenge of assessing them, *Nature Communications*, 13, 2208, <https://doi.org/10.1038/s41467-022-29838-9>, 2022.
- 1381 Meyer, H., Reudenbach, C., Wöllauer, S., and Naus, T.: Importance of spatial predictor variable
1382 selection in machine learning applications – Moving from data reproduction to spatial prediction,
1383 *Ecological Modelling*, 411, 108815, <https://doi.org/10.1016/j.ecolmodel.2019.108815>, 2019.
- 1384 Meyer, H., Milà, C., and Ludwig, M.: CAST: “caret” Applications for Spatial-Temporal Models, R package
1385 version 0.7.1, 2023.
- 1386 Microsoft Corporation and Weston, S.: doParallel: Foreach Parallel Adaptor for the “parallel” Package, R
1387 package version 1.0.17, 2022.
- 1388 Middelburg, J. J.: Reviews and syntheses: to the bottom of carbon processing at the seafloor,
1389 *Biogeosciences*, 15, 413–427, <https://doi.org/10.5194/bg-15-413-2018>, 2018.



- 1390 Middelburg, J. J.: Marine Carbon Biogeochemistry: A Primer for Earth System Scientists, Springer, Cham,
1391 Switzerland, 118 pp., 2019.
- 1392 Mitchell, P. J., Aldridge, J., and Diesing, M.: Legacy Data: How Decades of Seabed Sampling Can Produce
1393 Robust Predictions and Versatile Products, *Geosciences*, 9,
1394 <https://doi.org/10.3390/geosciences9040182>, 2019.
- 1395 Molnar, C., Bischl, B., and Casalicchio, G.: iml: An R package for Interpretable Machine Learning, *JOSS*, 3,
1396 786, <https://doi.org/10.21105/joss.00786>, 2018.
- 1397 Nellemann, C., Corcoran, E., Duarte, C. M., Valdés, L., De Young, C., Fonseca, L., and Grimsditch, G.: Blue
1398 Carbon: A Rapid Response Assessment., United Nations Environment Programme, GRID-Arendal,
1399 Norway, 2009.
- 1400 NRCan: Lakes, Rivers and Glaciers in Canada - Hydrographic Features - Natural Resources Canada,
1401 Topographic Data of Canada - CanVec Series, 2019.
- 1402 NRCan: Canada west coast topo-bathymetric digital elevation model - Natural Resources
1403 Canada/Department of Fisheries and Oceans, Open Canada, 2021.
- 1404 Pace, M. C., Bailey, D. M., Donnan, D. W., Narayanaswamy, B. E., Smith, H. J., Speirs, D. C., Turrell, W. R.,
1405 and Heath, M. R.: Modelling seabed sediment physical properties and organic matter content in the
1406 Firth of Clyde, *Earth System Science Data*, 13, 5847–5866, <https://doi.org/10.5194/essd-13-5847-2021>,
1407 2021.
- 1408 PANGAEA®: Data Publisher for Earth & Environmental Science, <https://doi.org/10.1594/PANGAEA>, 2022.
- 1409 Pebesma, E.: Simple Features for R: Standardized Support for Spatial Vector Data, *The R Journal*, 10,
1410 439–446, <https://doi.org/10.32614/RJ-2018-009>, 2018.
- 1411 Pebesma, E.: stars: Spatiotemporal Arrays, Raster and Vector Data Cubes, R package version 0.6-0, 2022.
- 1412 Pedersen, T. L.: patchwork: The Composer of Plots, R package version 1.1.2, 2022.
- 1413 Peña, M. A., Fine, I., and Callendar, W.: Interannual variability in primary production and shelf-offshore
1414 transport of nutrients along the northeast Pacific Ocean margin, *Deep Sea Research Part II: Topical
1415 Studies in Oceanography*, 169–170, 104637, <https://doi.org/10.1016/j.dsr2.2019.104637>, 2019.
- 1416 Philibert, G., Todd, B. J., Campbell, D. C., King, E. L., Normandeau, A., Hayward, S. E., Patton, E. R., and
1417 Campbell, L.: Updated surficial geology compilation of the Scotian Shelf bioregion, offshore Nova Scotia
1418 and New Brunswick, Geological Survey of Canada - Open file, 8911, .zip file,
1419 <https://doi.org/10.4095/330474>, 2022.
- 1420 Posit Team: RStudio: Integrated Development Environment for R, Posit Software, PBC, Boston, MA,
1421 2022.
- 1422 QGIS.org: QGIS Geographic Information System., QGIS Association, <http://www.qgis.org>, 2021.



- 1423 R Core Team: R: A language and environment for statistical computing., R Foundation for Statistical
1424 Computing, Vienna, Austria., <https://www.R-project.org/>, 2022.
- 1425 Raven, J.: Blue carbon: past, present and future, with emphasis on macroalgae, *Biology Letters*, 14,
1426 <https://doi.org/10.1098/rsbl.2018.0336>, 2018.
- 1427 Restrepo, G. A., Wood, W. T., Graw, J. H., and Phrampus, B. J.: A machine-learning derived model of
1428 seafloor sediment accumulation, *Marine Geology*, 440, 106577,
1429 <https://doi.org/10.1016/j.margeo.2021.106577>, 2021.
- 1430 Roy, M.-H. and Larocque, D.: Prediction intervals with random forests, *Stat Methods Med Res*, 29, 205–
1431 229, <https://doi.org/10.1177/0962280219829885>, 2020.
- 1432 Sala, E., Mayorga, J., Bradley, D., Cabral, R. B., Atwood, T. B., Auber, A., Cheung, W., Costello, C., Ferretti,
1433 F., Friedlander, A. M., Gaines, S. D., Garilao, C., Goodell, W., Halpern, B. S., Hinson, A., Kaschner, K.,
1434 Kesner-Reyes, K., Leprieur, F., McGowan, J., Morgan, L. E., Mouillot, D., Palacios-Abrantes, J.,
1435 Possingham, H. P., Rechberger, K. D., Worm, B., and Lubchenco, J.: Protecting the global ocean for
1436 biodiversity, food and climate, *Nature*, 592, 397–402, <https://doi.org/10.1038/s41586-021-03371-z>,
1437 2021.
- 1438 Seiter, K., Hensen, C., Schröter, J., and Zabel, M.: Organic carbon content in surface sediments—defining
1439 regional provinces, *Deep Sea Research Part I: Oceanographic Research Papers*, 51, 2001–2026,
1440 <https://doi.org/10.1016/j.dsr.2004.06.014>, 2004.
- 1441 Silge, J. and Mahoney, M.: *spatialsample: Spatial Resampling Infrastructure*, R package version 0.3.0,
1442 2023.
- 1443 Smeaton, C., Hunt, C. A., Turrell, W. R., and Austin, W. E. N.: Marine Sedimentary Carbon Stocks of the
1444 United Kingdom’s Exclusive Economic Zone, *Frontiers in Earth Science*, 9, 50,
1445 <https://doi.org/10.3389/feart.2021.593324>, 2021.
- 1446 Snelgrove, P. V. R., Soetaert, K., Solan, M., Thrush, S., Wei, C. L., Danovaro, R., Fulweiler, R. W., Kitazato,
1447 H., Ingole, B., Norkko, A., Parkes, R. J., and Volkenborn, N.: Global Carbon Cycling on a Heterogeneous
1448 Seafloor, *Trends in Ecology & Evolution*, 33, 96–105, <https://doi.org/10.1016/j.tree.2017.11.004>, 2018.
- 1449 Soontiens, N. and Allen, S. E.: Modelling sensitivities to mixing and advection in a sill-basin estuarine
1450 system, *Ocean Modelling*, 112, 17–32, <https://doi.org/10.1016/j.ocemod.2017.02.008>, 2017.
- 1451 Soontiens, N., Allen, S. E., Latornell, D., Le Souëf, K., Machuca, I., Paquin, J.-P., Lu, Y., Thompson, K., and
1452 Korabel, V.: Storm Surges in the Strait of Georgia Simulated with a Regional Model, *Atmosphere-Ocean*,
1453 54, 1–21, <https://doi.org/10.1080/07055900.2015.1108899>, 2016.
- 1454 Sothe, C., Gonsamo, A., Arabian, J., Kurz, W. A., Finkelstein, S. A., and Snider, J.: Large Soil Carbon
1455 Storage in Terrestrial Ecosystems of Canada, *Global Biogeochemical Cycles*, 36, e2021GB007213,
1456 <https://doi.org/10.1029/2021GB007213>, 2022.
- 1457 Soulsby, R. L.: Simplified calculation of wave orbital velocities, Report TR 155 - HR Wallingford, 1, 2006.



- 1458 Stephens, D. and Diesing, M.: Towards Quantitative Spatial Models of Seabed Sediment Composition,
1459 PLOS ONE, 10, e0142502, <https://doi.org/10.1371/journal.pone.0142502>, 2015.
- 1460 Sumner, M.: tidync: A Tidy Approach to “NetCDF” Data Exploration and Extraction, R package version
1461 0.3.0, 2022.
- 1462 Turner, J. T.: Zooplankton fecal pellets, marine snow, phytodetritus and the ocean’s biological pump,
1463 Prog. Oceanogr., 130, 205–248, <https://doi.org/10.1016/j.pocean.2014.08.005>, 2015.
- 1464 Van Rossum, G. and Drake, F. L.: Python 3 Reference Manual, CreateSpace, Scotts Valley, CA, 2009.
- 1465 VERRA: Methods for Monitoring of Carbon Stock Changes and Greenhouse Gas Emissions and Removals
1466 in Tidal Wetland Restoration and Conservation Project Activities (M-TW), VCS Module VMD0051,
1467 Sectorial Scope 14, 1, 2020.
- 1468 Wager, S., Hastie, T., and Efron, B.: Confidence Intervals for Random Forests: The Jackknife and the
1469 Infinitesimal Jackknife, Journal of Machine Learning Research, 15, 1625–1651, 2014.
- 1470 Wickham, H., François, R., Henry, L., Müller, K., and Vaughan, D.: Welcome to the {tidyverse}, Journal of
1471 Open Source Software, 4, 1686, <https://doi.org/10.21105/joss.01686>, 2019.
- 1472 Wilson, R. J., Speirs, D. C., Sabatino, A., and Heath, M. R.: A synthetic map of the north-west European
1473 Shelf sedimentary environment for applications in marine science, Earth Syst. Sci. Data, 10, 109–130,
1474 <https://doi.org/10.5194/essd-10-109-2018>, 2018.
- 1475 Wood, S. N., Pya, N., and Säfken, B.: Smoothing Parameter and Model Selection for General Smooth
1476 Models, Journal of the American Statistical Association, 111, 1548–1563,
1477 <https://doi.org/10.1080/01621459.2016.1180986>, 2016.
- 1478 Wright, M., N. and Ziegler, A.: {ranger}: A Fast Implementation of Random Forests for High Dimensional
1479 Data in {C++} and {R}, Journal of Statistical Software, 77, 1–17, 2017.
- 1480 Zhang, X., Chen, S., Xue, J., Wang, N., Xiao, Y., Chen, Q., Hong, Y., Zhou, Y., Teng, H., Hu, B., Zhuo, Z., Ji,
1481 W., Huang, Y., Gou, Y., Richer-de-Forges, A. C., Arrouays, D., and Shi, Z.: Improving model parsimony and
1482 accuracy by modified greedy feature selection in digital soil mapping, Geoderma, 432, 116383,
1483 <https://doi.org/10.1016/j.geoderma.2023.116383>, 2023.
- 1484